

1 **Controls on sill and dyke-sill hybrid geometry and propagation in the crust: The**
2 **role of fracture toughness**

3 **J. L. Kavanagh^{1*}, B. D. Rogers^{1,2}, D. Boutelier³ and A.R. Cruden⁴**

4 ¹ Department of Earth, Ocean and Ecological Sciences, University of Liverpool, Jane Herdman
5 Building, 4 Brownlow Street, Liverpool L69 3GP, UK.

6 ² Department of Geosciences, Physics of Geological Processes, University of Oslo, Oslo.

7 ³ School of Environmental and Life Science, University of Newcastle, Callaghan, NSW 2308,
8 Australia

9 ⁴ School of Earth, Atmosphere and Environment, Monash University, Clayton Campus,
10 Clayton, VIC 3800, Australia

11 *Corresponding author: Janine Kavanagh (janine.kavanagh@liverpool.ac.uk)

12 **Abstract**

13 Analogue experiments using gelatine were carried out to investigate the role of the mechanical
14 properties of rock layers and their bonded interfaces on the formation and propagation of
15 magma-filled fractures in the crust. Water was injected at controlled flux through the base of a
16 clear-Perspex tank into superposed and variably bonded layers of solidified gelatine.
17 Experimental dykes and sills were formed, as well as dyke-sill hybrid structures where the
18 ascending dyke crosses the interface between layers but also intrudes it to form a sill. Stress
19 evolution in the gelatine was visualised using polarised light as the intrusions grew, and its
20 evolving strain was measured using digital image correlation (DIC). During the formation of
21 dyke-sill hybrids there are notable decreases in stress and strain near the dyke as sills form,
22 which is attributed to a pressure decrease within the intrusive network. Additional fluid is
23 extracted from the open dykes to help grow the sills, causing the dyke protrusion in the
24 overlying layer to be almost completely drained. Scaling laws and the geometry of the
25 propagating sill suggest sill growth into the interface was toughness-dominated rather than
26 viscosity-dominated. We define K_{Ic}^* as the fracture toughness of the interface between layers
27 relative to the lower gelatine layer K_{IcInt} / K_{IcG} . Our results show that K_{Ic}^* influences the type
28 of intrusion formed (dyke, sill or hybrid), and the magnitude of K_{IcInt} impacted the growth rate
29 of the sills. K_{IcInt} was determined during setup of the experiment by controlling the temperature
30 of the upper layer T_m when it was poured into place, with $T_m < 24^\circ\text{C}$ resulting in an interface
31 with relatively low fracture toughness that is favourable for sill or dyke-sill hybrid formation.
32 The experiments help to explain the dominance of dykes and sills in the rock record, compared
33 to intermediate hybrid structures.

34 *Keywords:* dyke, sill, analogue experiment, gelatine, fracture toughness, magma intrusion

35 **1. Introduction**

36 Constraining the physical processes that control magma transport through the lithosphere is
37 fundamental in a wide range of geological contexts, from construction of the continental crust
38 (e.g. Annen et al. 2006) to understanding the tendency and triggers of volcanic eruptions
39 (Sigmundsson et al. 2010). Magma intrusion is much more frequent than magma eruption,
40 with intrusion to extrusion ratios ranging from 5:1 in oceanic areas to 10:1 in continental areas
41 (Crisp, 1984). At stratovolcanoes, it is estimated that only 10-20% of dykes reach the surface
42 (Gudmundsson 2002; Gudmundsson & Brenner 2005). Whether magma intrudes the crust to
43 form a magma chamber or transits directly to the surface to erupt will impact the style and
44 frequency of global volcanism and therefore the associated hazards (e.g. Loughlin et al., 2015).

45 Intrusive magmatic bodies can form a variety of geometries across a wide range of scales: from
46 dyke and sills, which are thin tabular magma intrusions that either cross-cut or intrude between
47 crustal layers, respectively, to plutons that have lower aspect-ratio and are built through the
48 accretion of smaller magma bodies (Glazner et al. 2004; Cruden & McCaffrey 2001; Coleman
49 et al. 2004). Magma ascends through the crust largely within fractures, interacting with crustal
50 heterogeneities (e.g. stratigraphic layering, faults, joints, and lithological contacts). Crustal
51 discontinuities may form a mechanical ‘interface’ between rock layers, and therefore a
52 structural weakness that could be exploited by migrating magmas. The majority of magmatic
53 intrusions do not culminate in surficial eruptions (Gudmundsson 2002; Gudmundsson &
54 Brenner 2005; Gudmundsson 1983); instead, many dykes go on to form sills at some critical
55 point during their propagation (e.g. Magee et al. 2013). Dykes are often associated with
56 extensional settings (e.g. Anderson 1938) and some of the largest sills on Earth are found in
57 rift-related sedimentary basins; they are important in the breakup of continents and the
58 production of flood basalts (e.g. Muirhead et al. 2014). Sills can help to improve petroleum
59 prospectivity (Malthe-Sørenssen et al. 2004; e.g. Gudmundsson & Løtveit 2014), can be a host

60 to diamondiferous kimberlite magma (Kavanagh & Sparks 2011; Gernon et al. 2012; J. L.
61 White et al. 2012), and are an important resource in mineral exploration (e.g. REE, Ni, Cu, Mo,
62 W, Sn, Au, Ag, Fe and platinum group elements (PGE); Barnes et al. 2016; Blundy et al. 2015;
63 Naldrett 2011).

64 Analogue modelling has proved to be an important tool in bridging the gap between field and
65 monitoring data of magma intrusion processes, to test hypotheses and identify the key
66 parameters that control magma ascent (see Rivalta et al. (2015) and Galland et al. (2015) for
67 reviews). Recent progress has been made to quantify the mechanical properties of gelatine and
68 its appropriateness as an analogue material to study magma intrusion in the crust (Kavanagh et
69 al. 2013). In this paper, we present methods to measure the fracture toughness of elastic gelatine
70 layers and the interface between layers, and use this to constrain the conditions leading to the
71 formation of dykes, sills and hybrid geometries in nature. Detailed quantification of the
72 evolving strain and stress in the elastic host material in the development of dyke-sill hybrid
73 structures is presented using the photo-elastic properties of gelatine and digital image
74 correlation (DIC) techniques. The importance of interfaces, as an example of a rock
75 discontinuity, in the development of hybrid intrusions is discussed with implications for
76 understanding magma ascent dynamics through the crust and the construction of large igneous
77 bodies.

78 **2. Theory and experimental framework**

79 *2.1. Hydraulic fractures*

80 The theory of rock fracture mechanics is fundamental to magma intrusion in the crust. Dykes
81 and sills can be considered as hydrofractures, i.e. rock fractures that are filled with, and formed
82 by, a pressurised fluid (magma) (see Rivalta et al. 2015 for a comprehensive review). Theory
83 states that the initiation of a hydrofracture occurs when the tensile strength of the host rock is

84 exceeded by the overpressure P_0 of the intruding magma. If there is a density contrast ($\Delta\rho$)
85 between the magma and the host then a buoyancy pressure P_b is generated across the vertical
86 extent of the intrusion (h):

$$87 \quad P_b = \Delta\rho gh \quad [1].$$

88 For dyke ascent, it is not the density contrast along the entire dyke length but the ‘local’
89 buoyancy at the ascending head region that is important (referred to in the literature as the
90 buoyancy length L_b , e.g. Taisne and Tait (2009) and Kavanagh et al. (2013)). An effective
91 buoyancy contribution may come from a vertical gradient in stresses acting on the intrusion
92 (Takada 1989; Lister & Kerr 1991b), though for sill propagation this is likely to be minimal.

93 A hydrofracture will propagate if the mode I stress intensity factor K_I at the crack tip, which is
94 a function of P_0 and the crack length L , exceeds a critical value known as the fracture toughness
95 K_{Ic} of the host material. The overpressure of the magma must reach or exceed the fracture
96 pressure P_f for the crack to grow:

$$97 \quad P_0 > P_f = \frac{K_{Ic}}{\sqrt{L\pi}} \quad [2].$$

98 Consequently, less overpressure is required for propagation as a crack grows in length.

99 In an isotropic material, the orientation and opening direction of a hydrofracture is determined
100 by the principle stresses acting on the volume of material. The crack will open towards the
101 minimum principal stress direction σ_3 with its length parallel to the maximum principal stress
102 direction σ_1 . In an anisotropic material, such as a rock with pre-existing fractures, then
103 discontinuities may be intruded by magma if the overpressure exceeds the normal stress acting
104 on them (Delaney et al. 1986).

105 *2.2. Crust and magma analogue materials*

106 Analogue experiments require the selection of carefully considered and appropriate materials
107 to ensure that they are geometrically, kinematically and dynamically scaled with respect to
108 nature (Hubbert 1937). Finding analogue materials that are ‘ideal’ is, however, not
109 straightforward; when studying dykes and sills the characteristics of both the host medium and
110 the intruding fluid need to be considered, and experimental limitations and compromises
111 commonly need to be made (Galland et al. 2015). Ideally the experiments should also allow
112 the dynamics of intrusion to be easily measured, to record the evolution of the subsurface
113 geometry and how it changes during growth.

114 In this study, pigskin gelatine was selected as the crust analogue material (Chanceaux &
115 Menand 2014; Daniels & Menand 2015; Fiske & Jackson 1972; Hyndman & Alt 1987;
116 Kavanagh et al. 2006; Kavanagh et al. 2015; Menand & Tait 2002; Rivalta et al. 2005; Taisne
117 & Tait 2011; Takada 1990). Gelatine is a viscoelastic material, exhibiting viscous and elastic
118 deformation in different proportions depending on concentration, temperature, age, strain or
119 strain rate (Di Giuseppe et al. 2009; Kavanagh et al. 2013; van Otterloo & Cruden 2016). At
120 low temperature (5-10°C), relatively short periods of time (tens of minutes) and for small
121 applied stresses gelatine can be considered to be an almost ideal-elastic material. The
122 mechanical properties of gelatine can be carefully controlled: its Young’s modulus evolves
123 with time and increases to a ‘plateau’ value, the magnitude of which is controlled by
124 concentration and defines the time after which the gelatine can be considered ‘cured’. Mixtures
125 of between 2 and 5 wt% gelatine scale well to crustal rocks for experiments of magma
126 intrusions in the crust (Kavanagh et al. 2013). Superposed layers of cured gelatine with well-
127 constrained mechanical properties can be variably bonded, with either a strong or weak bond
128 relative to the fracture toughness of the gelatine layers (see Kavanagh et al. 2015). Gelatine is
129 a transparent substance, and as such the injection of fluid and growth of experimental intrusions

130 can be observed in real time. Furthermore, it is photoelastic so the relative stresses revealed by
131 birefringence colours can be observed using polarized light (e.g. Taisne & Tait 2011).

132 Water is an appropriate analogue for magma in these experiments as it has low viscosity, and
133 during injection it has low Reynolds number (Kavanagh et al. 2006). The density of water is
134 also closely matched to gelatine, so buoyancy is negligible. Glycerine or glucose can be added
135 to water to increase its density and viscosity, and the effects of solidification on intrusion
136 dynamics can also be considered using temperature-dependent materials (e.g. Taisne & Tait
137 2011; Chanceaux & Menand 2014), but such variations are beyond the scope of this study.

138 *2.3. Measurement and control of gelatine properties*

139 *2.3.1. Young's modulus E of gelatine layers*

140 The Young's modulus of a gelatine layer was measured, when possible, immediately prior to
141 an experiment being carried out by applying a load of known dimensions and mass to the free-
142 surface and measuring the resulting deflection (Kavanagh et al. 2013):

$$143 \quad E = \frac{mg(1-\nu^2)}{2ab} \quad [3],$$

144 where m is the mass of the load, g is acceleration due to gravity, ν is Poisson's ratio (0.5 for
145 gelatine), a is the radius of the load and b is the deflection of the top surface of the gelatine due
146 to the load (see Kavanagh et al. 2013). Two loads were applied sequentially, and the average
147 E reported (see Table 1 for load properties). Kavanagh et al. (2013) established that there is a
148 linear relationship between gelatine concentration (wt%) and E , provided sufficient curing time
149 has elapsed. In layered experiments, the Young's modulus of the lower layer E_1 and the rigidity
150 ratio of upper layer relative to lower layer E_2 / E_1 cannot be measured directly and so these are
151 estimated from concentration alone; however, the Young's modulus of the upper layer E_2 is
152 measured.

153 *2.3.2 Fracture toughness measurements K_{IcG} and K_{IcInt}*

154 The fracture toughness K_{Ic} is a measure of a material's ability to resist fracture. The method to
155 calculate K_{Ic} depends on the injection method of fluid into the gelatine layers, either a peristaltic
156 pump at a constant volumetric flux (Q) (Kavanagh et al. 2015) or using a head pressure P_h
157 (Kavanagh et al. 2013). The experiments we present here use a peristaltic pump to inject fluid
158 into the gelatine solids.

159 The elastic pressure P_e (Lister & Kerr 1991a), equivalent to the overpressure P_0 , required to
160 open the fluid-filled fracture is calculated as follows:

161
$$P_e = \frac{E}{2(1-\nu^2)} \frac{H}{L} \quad [4]$$

162 where H is the thickness and L is the length of the fluid-filled fracture. When a peristaltic pump
163 injects the fluid, K_{Ic} of the gelatine layers and interface can be calculated provided it can be
164 demonstrated that the fracture pressure (equation 2) and elastic pressure (equation 4) are in
165 equilibrium $P_f = P_e$ (Kavanagh et al. 2015):

166
$$K_{Ic} = \frac{EH\sqrt{\pi}}{2(1-\nu^2)\sqrt{L}} \quad [5].$$

167 The volumetric flux Q is measured as the volume of outflow from the injector per second.

168 *2.3.3. Interface fracture toughness control: gelatine mixture temperature T_m*

169 During preparation of the experiment, the temperature T_m of the upper gelatine layer is recorded
170 when it is poured onto the solidified lower layer. The temperature of the lower layer was ~5
171 °C when the upper layer was poured into place. Previous work suggests that the mechanical
172 properties of the interface between the gelatine layers is controlled during experiment
173 preparation by varying the temperature contrast between the lower cold, solid gelatine layer
174 and the new hot gelatine layer when it is emplaced (Kavanagh et al 2006, 2015). It has been
175 suggested that a 'strong' interface is produced if the upper layer is poured into place at a

176 temperature that is several degrees higher than the gelling temperature of the lower layer (T_{gel}
177 $\sim 20^{\circ}\text{C}$), due to it temporarily melting the lower layer and welding to it. In contrast, when layer
178 2 is emplaced at a temperature close to T_{gel} a ‘weak’ interface is produced as minimal melting
179 of the lower layer occurs.

180 **3. Methodology**

181 *3.1. Experiment preparation and setup*

182 Preparation of the gelatine analogue experiments involves production of mixtures of specified
183 concentration (X wt%) and temperature (T_m °C). The gelatine was prepared by dissolving a
184 measured quantity of pig-skin gelatine powder (260 bloom, 20 mesh, from Gelita) in hot
185 distilled water (~ 90 °C) to a specified concentration (see Table 2). The majority of the
186 experiments had the same gelatine concentration for layer 1 and layer 2 (2.5 wt%), though one
187 experiment had a slightly more concentrated upper layer (MOPIV6 layer 2: 3.0 wt%). The hot
188 gelatine mixture was then placed into a clear-Perspex tank, and all bubbles were removed from
189 the surface. Two types of clear-Perspex container were used (see Figure 1), either a ‘large’
190 square-based tank (measuring $40 \times 40 \times 30$ cm³) or a ‘small’ cylindrical tank (15 cm diameter
191 and 20 cm height). To inhibit the collection of any condensation that might be formed onto the
192 gelatine surface during the cooling process, some experiments had oil poured onto the liquid
193 gelatine prior to it being put into a refrigerator at 5 °C to cool. This oil was then completely
194 removed prior to layer 2 being emplaced. Otherwise, the container was covered with plastic
195 film and the tank moved to the refrigerator. Once layer 1 had ‘gelled’ the next layer was
196 prepared using the same method. Experiments were performed by injecting dyed water into the
197 base of the tank via a tapered-injector using a peristaltic pump (controlled volumetric flux;
198 Figure 1). Rheometer data presented in Kavanagh et al. (2015) suggests that gelatine solids
199 behave elastically at these experimental conditions. The initial stress conditions were

200 hydrostatic and experimental variables included the size of container, rigidity contrast (E_2/E_1)
201 and T_m (see Tables 2 and 3). High-definition video cameras placed around the experimental
202 tank recorded the growth of the resulting experimental intrusions.

203 *3.2. Mapping stress and strain evolution in gelatine: Photoelasticity and digital image*
204 *correlation (DIC)*

205 A set of polarizing plates were attached to the outside of the tank to visualise stress changes in
206 the gelatine host as it was injected by water. Experiments were viewed with polarised light
207 (Figure 1B) where colour fringes indicate qualitative stress perturbations (e.g. Taisne & Tait
208 2011).

209 Strain evolution was measured quantitatively in the experiments using digital image correlation
210 (DIC) techniques (Kavanagh et al. 2015). In the experiments presented here, a frequency
211 doubled Nd:YAG laser sheet was triggered from above, illuminating fluorescent seeding
212 particles (PMMA-RhB, 20-50 μm , density 0.98 g/cc) added to the gelatine during its
213 preparation (see Figure 1A and Kavanagh et al. (2015)). The thin laser sheet (approximately
214 1 mm thick) illuminated a vertical 2-dimensional xz-plane through the experiment, and
215 intersected the centre of the tank (the point of injection). A CCD camera (LaVision Imager
216 Pro X 4M, 2048 x 2048 pixel resolution) recorded images of the fluoresced particles,
217 synchronised with each laser pulse. Images were recorded at 2 Hz for up to 60 minutes. A
218 532-546 nm pass band filter in front of the camera lens was used to eliminate stray reflections
219 of laser light.

220 Processing of the laser-fluoresced images was carried out using LaVision DaVis 8 software.
221 The field of view analysed was 40 x 30 cm^2 and the image resolution was approximately 5
222 pixels/mm. The recorded images were sub-sampled to 5-second intervals, and cross-
223 correlation between successive images ‘pattern matched’ the fluoresced passive tracer particles

224 to calculate displacement vectors within the gelatine. The analysis window-size was 64 x 64
225 pixels with an overlap of 87%, and a multi-pass filter with decreasing window size allowed
226 high precision (sub-pixel) and high resolution measurements of the incremental and cumulative
227 displacements to be calculated (e.g. Adam et al. 2005; Schrank et al. 2008; Kavanagh et al.
228 2015). When gelatine deforms elastically, the measured strain correlates with stress and this
229 relationship is quantified using rheometric data (Kavanagh et al. 2015).

230 **4. Results**

231 In total 11 experiments were carried out (Table 2), primarily varying the size of the experiment
232 (large or small tank), the temperature at which layer 2 was emplaced (T_m), and the concentration
233 of the gelatine layers (subscripts 1 and 2 refer to the lower and upper layers, respectively). The
234 layer thickness (D_1 and D_2), layer 2 curing time (t), gelatine temperature at the time the
235 experiment was run (T) and interface type (oiled or cling-wrap) was also recorded. The
236 Young's modulus of the gelatine was measured to be ~5000-8800 Pa, which scales to ~0.3-4.4
237 GPa in nature (Kavanagh et al. 2013); this value is comparable to typical sedimentary rock
238 layers, but is towards the lower end of values anticipated for sedimentary rocks at depth.

239 A range of sheet-intrusion geometries were produced in the experiments, including dykes, sills,
240 and dyke-sill hybrids (Table 2). Sills were formed when the ascending dyke quickly turned to
241 form a sill when reaching the interface. Erupted dyke fissures occurred when the ascending
242 dyke cut across the interface between the layers and ascended to erupt at the surface.
243 Intermediate dyke-sill hybrid structures occurred when the ascending dyke crossed the
244 interface but also intruded it. In these cases, the dyke protrusion that crossed the interface did
245 not go on to erupt. Similar structures have been produced in previous studies (e.g. Kavanagh
246 et al., 2006, 2015), but in section 4.1 we focus on the formation of the less studied and relatively
247 poorly understood dyke-sill hybrid structures.

248

4.1. Mechanics of dyke-sill hybrid intrusion formation and growth

249

250

251

252

253

254

255

Dyke-sill hybrid intrusions were produced five times in the experiments. Figure 2 shows a series of photographs of an experiment where a dyke-sill hybrid formed (LBR2). The vertical penny-shaped dyke intrusion first penetrated through the lower gelatine layer and then into the upper gelatine layer, and very shortly afterwards intruded the interface forming two distinct sills at the dyke's lateral tips (Figure 2A). The two sills grew quickly as they spread out into the interface between the gelatine layers (Figure 2B). The sills subsequently merged together and with the dyke margins at the interface to create the full hybrid structure (Figure 2C).

256

257

258

259

260

261

262

263

264

265

Video Figure 3 shows a hybrid intrusion growth viewed with polarised light, illustrating qualitative stress perturbations in the gelatine by the development and movement of colour fringes. As the dyke ascended through the lower gelatine layer stresses were concentrated at the head region, displaying the typical “bow tie” stress distribution expected during crack tip propagation in an elastic material (e.g. Pollard & Johnson 1973). Stresses then accumulated along the entire interface plane as it was approached by the intrusion. When the dyke crossed the interface, stress remained concentrated at the dyke tip as it protruded into layer 2. Shortly afterwards a sill formed by intruding the interface, and stresses were then concentrated at the growing sill margin. As the sill grew, stresses appear to be gradually reduced around the dyke protrusion in layer 2 but are difficult to see in layer 1.

266

267

268

269

270

271

272

Digital image correlation (DIC) was carried out to quantify strain changes in the gelatine as a dyke-sill hybrid intrusion was formed. During injection of the fluid, measurements were made within a 2-dimensional vertical plane through the gelatine solid that was illuminated by the laser sheet oriented perpendicular to the strike-direction of the feeder dyke. Video Figure 4 is a compilation of frames recorded during a dyke-sill hybrid experiment (MOPIV6) and is the ‘raw’ data used in the DIC analysis. Video Figure 5 presents the processed data, plotting horizontal incremental strain (elongation) ϵ_{xx} calculated at 5-second intervals within the plane

273 of the laser sheet. Key time intervals of significant changes in ε_{xx} during dyke-sill hybrid
274 formation are shown in Figure 5A-F. During the initial ascent of the dyke through gelatine
275 layer 1, incremental strain accumulated at the small tip-region of the dyke, and displacement
276 vectors indicate progressive opening of the fluid-filled crack; at 25-30 seconds after the start
277 of injection ε_{xx} had a maximum value of 23 % (Figure 5A). The dyke reached the interface
278 between the gelatine layers at 145 – 150 seconds; at this time ε_{xx} had reduced to a maximum
279 value of 1.7 % and strain was more distributed along the length of the dyke (Figure 5B). At
280 this time a small amount of strain had also accumulated within gelatine layer 2 directly above
281 the dyke. Subsequently the dyke propagated across the interface into layer 2 at 315-320 s, with
282 strain continuing to be concentrated in a small tip-region but with a slightly increased
283 maximum $\varepsilon_{xx} \sim 2.3$ % (Figure 5C). Sill formation occurred at 330-335 s and it was followed
284 by a rapid decrease in horizontal incremental strain in the gelatine around the feeder dyke,
285 shown by negative ε_{xx} values (Figure 5D). However, incremental strain continued to
286 accumulate simultaneously in the dyke protrusion in layer 2, with maximum values of 1.7 %.
287 As sill propagation continued, the feeder dyke in layer 1 continued to contract and was
288 associated with increasingly negative incremental strains in the adjacent gelatine (ε_{xx} reduced
289 to -3.0 %) with a small amount of positive strain remaining at the dyke tip in layer 2 (Figure
290 5E). The final stages of sill growth caused the dyke protrusion in layer 2 to also contract, with
291 negative incremental strains distributed along the entire dyke (at 340 – 345 s, Figure 5F).

292 To determine the evolution of total strain e_{xx} during dyke-sill hybrid formation an experiment
293 was analysed using DIC in a 5 mm x 5 mm square area adjacent to the centre of the feeder dyke
294 in the lower layer (MOPIV6). In Figure 6, the results from this analysis are compared with a
295 sill-formation example from Kavanagh et al. (2015) (there called Exp 5). The Kavanagh et al.
296 (2015) experiment was prepared in the same way as MOPIV6, has the same injection flux and
297 a weak interface but $E_2 = E_1$. The two experiments showed similar evolution in e_{xx} with four

298 phases of intrusion growth identified. In both experiments, the area monitored experienced a
299 gradual increase in total strain as the dyke propagated towards and then beyond it. Secondly,
300 in both experiments sill formation caused a rapid contraction of the feeder dyke and a rapid
301 decrease in e_{xx} . Thirdly, as the sills grew their feeder dykes continued to contract and total
302 strain continued to decrease. At the moment the injection pump was turned off there was a
303 small and rapid additional decrease in e_{xx} detected in both experiments. However, with a
304 maximum total strain of $\sim 35\%$ compared to $\sim 50\%$, the dyke-sill hybrid-forming experiment
305 reached a lower maximum total strain than the sill-forming experiment. The moment of sill
306 formation occurred simultaneously in the two experiments and the rate of decrease in e_{xx} was
307 identical, but overall the accompanying rapid decrease in total strain at sill formation was
308 greater in magnitude in the sill-forming experiment at 33% (50% down to 17%) compared to
309 15% (35% down to 20%) in the dyke-sill hybrid experiment.

310 *4.2. Toughness-dominated or viscosity-dominated propagation?*

311 There is some discussion in the literature regarding the nature of sill propagation dynamics,
312 when intrusion occurs into a weak boundary (or interface) between elastic layers. For dykes it
313 has been established in gelatine-based analogue experiments that propagation occurs in the
314 fracture toughness-dominated regime such that $P_0 \sim P_f$ (e.g. Menand & Tait 2002). However,
315 some studies have suggested that sill propagation dynamics could be viscosity-dominated such
316 that instead $P_0 \sim P_v$, where P_v is the viscous pressure (e.g. Kavanagh et al. 2006; Chanceaux
317 and Menand, 2016).

318 *4.2.1 Equilibrium length and thickness ratios*

319 It has been demonstrated in previous studies that the expected length and thickness of a
320 pressurized fluid-filled crack intruding an elastic material can be calculated assuming a
321 pressure equilibrium that is either fracture toughness- or viscosity- dominated. The toughness

322 equilibrium model assumes the fracture pressure P_f (equation 2) and elastic pressure P_e
323 (equation 4) are equal for a given injection flux (for details see Appendix of Kavanagh et al.
324 2015), and from this K_{Ic} can be calculated (equation 5). Instead, the viscosity equilibrium model
325 assumes that the elastic pressure P_e is equal to the viscous pressure P_v for a given injection flux
326 (Chanceaux and Menand, 2016):

$$327 \quad P_v = \frac{12\mu L^2}{H^2 t} \quad [6]$$

328 where μ is the viscosity of the intruding fluid, H is the thickness and L the length of the intrusion
329 at time t after sill injection.

330 Figure 7 plots dyke length against time for several experiments where fluid was injected with
331 constant flux in a large tank (A) and small tank (B). The toughness equilibrium model is shown
332 and defines the expected change in the length of the dyke (+/- 10%). Figure 7A shows that in
333 the large-tank experiments the length evolution of the dykes in layer 1 indicates they all formed
334 in toughness-dominated pressure-equilibrium as they fall within 10% error of the model.
335 Figure 7B shows that all small tank experiments except SBR21 can also be considered to have
336 formed in equilibrium within error, although the fit of the data to the model curves is not as
337 good in the small tanks compared to the large tank experiments. These results suggest that
338 dyke propagation in our experiments occurred in the toughness-dominated regime.

339 Figure 8 plots sill length, thickness and length/thickness ratio of a representative sill-forming
340 experiment MOPIV9, where the intrusion was imaged using a laser sheet positioned through
341 the centre of the intrusion and so the geometry measurements have a small error. Model length,
342 thickness and their ratio over time are plotted assuming propagation was toughness- or viscous-
343 dominated. Figure 8A) shows the sill length lies almost equally between that modelled by the
344 two regimes, being initially quite close to the viscous-dominated model but moving
345 progressively towards the toughness-dominated expected length with time. However, the

346 graphs of sill thickness (Figure 8B) and the length/thickness ratio (Figure 8C) show these are
347 consistently closer to that expected by the toughness-dominated model through the sill growth.
348 It is clear that the dynamics of sill propagation in our experiments are complex, however the
349 results indicate that they are overall better described by the toughness-dominated model.

350 4.2.2 Fracture toughness calculations K_{IcG} and K_{IcInt} and relationship with T_m

351 Given that Figures 7 and 8 indicates that it is valid to assume $P_e \sim P_f$ for both dyke and sill
352 propagation in several of the analogue experiments, and therefore that propagation was overall
353 toughness-dominated, we conclude that it is appropriate to use equation 5 to calculate the
354 fracture toughness of the lower gelatine layer (K_{IcG}) and the interface between gelatin layers
355 (K_{IcInt}). The results of these calculations are shown in Table 3 and use the Young's modulus
356 of the upper layer E_2 as well as the length and thickness measurements of the dyke taken
357 immediately prior to sill formation for K_{IcG} and immediately after sill inception for K_{IcInt} .

358 In most cases it has been possible to calculate K_{IcG} , however it is only experiments which were
359 sill-forming or dyke-sill hybrid-forming that it has been possible to calculate K_{IcInt} . Where it
360 was possible to calculate K_{IcG} the average was found to be $102 \text{ Pa m}^{0.5}$, which is consistent with
361 previously published values of 2.5 wt% gelatine solids tested at comparable experimental
362 conditions (Kavanagh et al. 2013; Kavanagh et al. 2015). The mean K_{IcG} was slightly smaller
363 for the large tank experiments at $103 \text{ Pa m}^{0.5}$ compared to the small tank experiments at 106 Pa
364 $\text{m}^{0.5}$ (when dyke-sill hybrids or sills were formed and $E_2 = E_1$). We note that an alternative
365 equation to calculate fracture toughness of gelatine solids $K_{Ic} = 1.4(+/- 0.1) \sqrt{E}$, proposed by
366 Kavanagh et al. (2013), produces very similar values; calculations using an estimated E , based
367 on the assumption layer 1 has cured, rather than measured E_2 give similar but slightly higher
368 values of K_{IcG} . In comparison, the mean fracture toughness of the interface K_{IcInt} was calculated
369 as $52 \text{ Pa m}^{0.5}$ with a median of $55 \text{ Pa m}^{0.5}$, and it was always less than K_{IcG} .

370 K_{IcG} and K_{IcInt} of large-tank experiments that formed sills or dyke-sill hybrids are plotted
371 against T_m in Figure 9. The results show that K_{IcInt} is positively correlated with T_m (coefficient
372 of determination $r^2 = 0.48$) following the empirical relationship:

$$373 \quad K_{IcInt} = 12.1T_m - 197 \quad [7].$$

374 This suggests that K_{IcInt} can be calculated experimentally based purely on measurement of T_m .
375 The intersection of the K_{IcInt} model with the mean K_{IcG} identifies an upper bound for K_{IcInt} that
376 can be achieved in the experiments when T_m is between 24-25 °C (for a 2.5wt concentrated
377 gelatin at 5 °C).

378 *4.2.3 Fracture toughness ratio impact on intrusion geometry*

379 To explore the parameter space further, we introduce the normalized fracture toughness $K_{Ic}^* =$
380 K_{IcInt} / K_{IcG} and plot this against T_m and according to the type of intrusion formed (Figure 10).
381 Two distinct fields are evident in Figure 10: 1) a dyke-forming region where $K_{Ic}^* \geq 1$ and T_m
382 > 24 °C, and 2) a sill-forming or dyke-sill hybrid-forming field where $K_{Ic}^* < 1$, where lower
383 K_{Ic}^* values tend to be associated with sill formation. Calculated values of K_{Ic}^* are shown in
384 Table 3. An estimated value of 1 was assigned to dyke-forming experiment SBR18, as the
385 interface was not intruded its fracture toughness could not be measured directly. Potentially
386 the conditions where $K_{Ic}^* > 1$ could be explored experimentally if the upper layer were stiffer
387 than the lower layer and the interface was not intruded. However, experiment MOPIV6 which
388 had $E_2 > E_1$ was dyke-sill hybrid-forming and had $K_{Ic}^* < 1$ (Table 3). In none of our
389 experiments did we measure or infer $K_{Ic}^* > 1$, however fracture toughness tests on rock
390 interfaces have suggested this could be realised in nature (Kavanagh & Pavier 2014) so would
391 be interesting to explore in future experiments.

392 Fracture toughness of the gelatine layers and their interface not only influenced the geometry
393 of intrusions that were formed, but also the propagation dynamics of the sill growth. This is

394 shown in Figure 11 where the change in length of sill is plotted against time for two sill
395 experiments (LBR4 and LBR5) and a dyke-sill hybrid experiment (LBR6). In all three
396 experiments there is an initial stage of rapid sill growth for up to ~40 seconds, and then a second
397 phase of slower growth until the sill reached the tank wall. Sill growth was asymmetrical and
398 predominantly towards one tank wall. During the initial stages of sill formation, faster growth
399 rates were associated with interfaces that had lower fracture toughness (Figure 10). The
400 mechanical properties of the interface have therefore not just determined the type of intrusion
401 formed (sill, hybrid, or dyke) but has also affected the growth dynamics of the sill as the
402 interface is intruded. A change in sill growth rate was indicated by the change of slope on the
403 distance-time plot; this may be due to interaction with the tank walls, or instead marks the time
404 when the sill began to strongly interact with the free surface as its length became greater than
405 the layer thickness (D_2) (see Bunger & Cruden 2011).

406 4.3 *Scaling laws of toughness- or viscosity- dominated regimes*

407 The existence of viscosity-dominated and toughness-dominated regimes for penny-shaped sills
408 is well established in the mechanics and hydrofracture literature. To further explore the nature
409 of sill propagation in our experiments we apply the model of Savitski and Detournay (2002)
410 who examine a penny-shaped hydrofracture propagating in an infinite elastic region. This
411 model is similar in approach to Bunger and Cruden (2011), who study the emplacement of
412 shallow sills under a thin, plate-like overburden, and is equivalent to comparing pressure scales
413 to calculate when during intrusion growth the dynamics are viscosity- or toughness-dominated.

414 Savitski and Detournay (2002) define three parameters:

$$415 \mu' = 12\mu \quad [8]$$

$$416 E' = \frac{E}{1-\nu^2} \quad [9]$$

417
$$K' = 4K_{Ic} \sqrt{\frac{2}{\pi}} \quad [10]$$

418 introducing a dimensionless fracture toughness K :

419
$$K = K' \left(\frac{t^2}{\mu^{15} Q_0^3 E^{13}} \right)^{1/18} . \quad [11]$$

420 According to Savitski and Detournay (2002), the viscosity-dominated regime occurs when $K \leq 1$
 421 and toughness-dominated when $K \geq 3.5$.

422 Applying Savitski and Detournay's (2002) model to study dyke propagation in our experiments
 423 we use an estimate of $K_{Ic} = 119 \text{ Pa m}^{-0.5}$, based on an independent estimate of fracture toughness
 424 of a 2.5 wt% gelatine from Kavanagh et al. (2013), to calculate that in our experiments $K > 7$
 425 when $E = 5550 \text{ Pa}$. Considering sill propagation along an interface, we then calculate sill
 426 propagation was in the toughness-dominated regime where $K > 3.5$ even if we assume $K_{IcInt} =$
 427 $16 \text{ Pa m}^{-0.5}$ when $E = 5550 \text{ Pa}$ and $K_{IcInt} = 23 \text{ Pa m}^{-0.5}$ when $E = 8880 \text{ Pa}$. Similarly to the
 428 equilibrium length and thickness models described in Section 4.2.1, these calculations support
 429 our assumption that sill propagation in the experiments was toughness-dominated.

430 *4.4. Boundary conditions: Experiment tank size*

431 Boundary effects were explored by considering the size of tank in which the experiment was
 432 carried out. As fluid was intruded into the gelatine to form dykes and sills it displaced the host
 433 gelatine, and in the large-tank experiments the amount of displacement due to the dyke
 434 intrusion was very small in comparison with the size of the container and so boundary effects
 435 were minimal. However, in the small tank experiments this displacement was relatively large
 436 and when the sill grew along the interface it very quickly reached the tank wall. We would
 437 therefore recommend that the large tank size be the minimum used in future experiments, so
 438 that a wider range of experimental variables and intrusion propagation dynamics can be
 439 explored.

440 **5. Discussion**

441 *5.1. The influence of crustal heterogeneity on magma intrusion dynamics*

442 There is good evidence from field observations, geophysical surveys, active monitoring of
443 magma intrusion and numerical models that mechanical layering and rock heterogeneity play
444 an important role in controlling the geometry of magma intrusions in the crust and whether
445 magmas go on to erupt (e.g., Le Corvec et al. 2015; Geshi et al. 2012; Kavanagh et al. 2006;
446 Gudmundsson 2011; Taisne & Jaupart 2009). The geometry of the intrusions produced in the
447 gelatine analogue experiments presented here are much simpler than in nature, yet we have
448 produced a range of different intrusion geometries whose form systematically depends on the
449 mechanical properties of the intruded host and especially their contacts. In particular, the
450 importance of the fracture toughness contrast between the intruded layers and their interface,
451 K_{Ic}^* , is identified as a key parameter in determining what type of intrusion forms and how it
452 grows, when the intruded layers are of equal rigidity.

453 The tendency for magma-filled fractures to utilise rock discontinuities in nature is likely to be
454 variable due to their range of mechanical properties. The Earth's crust is inherently
455 heterogeneous across many scales, comprising mechanically distinct layers that are variably
456 bonded (Kavanagh & Pavier 2014), and in sub-volcanic areas it has been postulated that most
457 intrusions do not reach the surface (Gudmundsson 1983). A recent survey of a well-exposed
458 sub-volcanic plumbing system in Utah found that >92% of intrusive material in the field
459 occurred in sill-like bodies (Richardson et al. 2015) that had formed between layers of
460 sandstone and siltstone. In intra-plate settings, the alignment of volcanic vents along pre-
461 existing structures (joints or faults) indicates these have been used to assist magma ascent to
462 eruption (e.g. Le Corvec et al. 2013). Our results suggest that when the fracture toughness of a
463 rock interface is lower than that of the adjacent rocks, sills and dyke-sill hybrids will form
464 rather than dykes that erupt. Mechanical discontinuities and crustal heterogeneity are therefore

465 highly significant in the preferential formation of sills and dyke-sill hybrids and the
466 development of sub-volcanic plumbing systems.

467 *5.2. Dyke-sill hybrids in nature, implications for large magma body growth*

468 Dyke-sill transitions and dyke-sill hybrid structures are only rarely reported in field studies,
469 perhaps due to the lateral extent of sills being very large in comparison to their feeder dyke and
470 so less likely to be exposed. They are also difficult to image in seismic reflection surveys.
471 Despite this, dyke-sill hybrids have been observed in nature in exceptional exposures of
472 intrusive networks in Patagonia. Figure 12 shows photographs of felsic dyke-sill hybrids and
473 surrounding dykes and sills that have intruded a folded turbidite sequence in the Torres del
474 Paine National Park, Chile. These intrusions are part of the Torres del Paine Intrusive Complex
475 (TPIC) and have intruded rocks that comprise intercalated sandstone, siltstone and mudstone
476 layers. The heterogeneity of the host rock may have played an important role in the
477 development of the intrusive magma structures. The intrusions have protruded from the roof
478 of a large granite laccolith body which has intruded the rock layers below (see bottom of Figure
479 11A). The close proximity of the small dyke-sill hybrids with the large igneous body suggests
480 they are associated. This is supported by mapping and geochronology of the TPIC, which
481 indicates that the laccolith was built by incremental growth (e.g. Leuthold et al., 2012) and the
482 accumulation of dykes, sills and hybrid structures within the crust. So-called ‘christmas tree’
483 laccolith structures (e.g. Corry, 1988; Rocchi et al. 2010) may have formed in a similar way.
484 Our results suggest that the relative scarcity of hybrid intrusion geometries in nature could be
485 explained by the mechanical conditions that enable their formation being relatively difficult to
486 achieve, requiring rock layers that have similar Young’s modulus and similar layer and
487 interface fracture toughness. By better constraining the conditions for dyke, sill and hybrid
488 formation we may also provide insights on the formation and growth of larger magma bodies
489 (Annen et al. 2015).

490

5.3. Pressure changes during sill and dyke-sill hybrid formation

491 In a previous study, Kavanagh et al. (2015) demonstrated how strain evolution is correlated
492 with stress changes in experiments where gelatine deforms elastically. Our results support this
493 finding, as the distribution of stress change in the gelatine observed using polarised light (Video
494 Figure 3) is very similar to the pattern of strain evolution quantified using DIC (Video Figure
495 4 and Figure 5). The controlled-flux experiments demonstrate that during dyke-sill hybrid
496 growth, fluid extracted from both the feeder dyke in the lower layer and the upper layer dyke
497 protrusion contribute to sill growth. Assuming the fluid is coupled to the gelatine at the dyke
498 margin, stress changes in the gelatine can be related to pressure changes in the fluid. In the
499 experiments, dyke-sill hybrid formation coincided with a decrease in total strain in the gelatine
500 host, and therefore a decrease in fluid pressure within the intrusion as the sill formed (Video
501 Figure 4, Figure 5, Figure 6). This pressure decrease was documented early in the formation
502 of the hybrid structure, when the influence from the lateral boundary conditions was minimal,
503 and amounted to ~40% reduction in pressure. However, this pressure reduction is less than has
504 been previously documented in experimental studies of sill formation events (Kavanagh et al.
505 2015) where >60% pressure reduction has been measured.

506 In nature, pressure changes in magma can be significant with the potential to destabilise the
507 dyke-sill network if gas exsolution and crystallisation is induced (e.g. Tarasewicz et al. 2012).
508 The dyke-sill hybrid experiment (MOPIV6) had a more rigid upper layer and a lower fracture
509 toughness interface than the sill-forming experiment (see Kavanagh et al. 2015). This
510 mechanical heterogeneity of the host gelatine, the development of a hybrid structure, and the
511 impact of the dyke protrusion in the upper layer may have contributed to smaller pressure
512 fluctuations in the dyke-sill hybrid experiments compared to the sill-forming experiments.

513 Our results suggest that the mechanical properties of the rock layers and their discontinuities
514 are likely to influence the magnitude of pressure changes experienced by intruding magmas.

515 The mechanical conditions that induce magmatic pressure variations will be of significance for
516 constraining the conditions that may enhance gas exsolution, increase magma ascent rates and
517 therefore potentially lead to volcanism. The mechanical heterogeneity of crustal rock layers
518 and their discontinuities should therefore be considered as a key parameter in models of magma
519 ascent through the crust.

520 **6. Conclusions**

521 Dyke fissures, sills and dyke-sill hybrids were formed in a series of gelatine analogue
522 experiments to study magma ascent through a layered-elastic crust. When the intruded layers
523 were of equal rigidity, we defined K_{Ic}^* as the relative magnitude of fracture toughness of the
524 gelatine layers K_{IcG} and their bonded interface K_{IcInt} . Dyke formation occurred when $K_{Ic}^* \geq 1$,
525 whereas dyke-sill hybrids or sills formed when $K_{Ic}^* < 1$. Sill formation was associated with
526 relatively low values of K_{IcInt} and K_{Ic}^* . The mixture temperature T_m of gelatine layer 2 during
527 preparation of the experiment correlates positively with K_{IcInt} , and an upper limit for K_{IcInt} is
528 reached when T_m is 24-25 °C. The photo-elastic properties of gelatine allowed the stress
529 development and evolution to be visualised during the growth of the intrusions, which correlate
530 well with strain evolution in the gelatine host mapped using DIC. Dyke-sill hybrid formation
531 was associated with a significant fluid pressure decrease, though the effect was less than in sill-
532 forming experiments. The experiments highlight the importance of mechanical layering and
533 heterogeneities, such as interface properties, on the geometry and propagation of magmatic
534 intrusions and their tendency to erupt. The relative scarcity of dyke-sill hybrid intrusions in
535 nature could be explained by the conditions required for their formation being unusual or
536 difficult to achieve, and instead the mechanical state of the crust leads to the preferential
537 development of either dykes or sills.

Acknowledgments

JK acknowledges a Royal Society Research Grant (RG130771), BR and JK thank support from the University of Liverpool. DB and AC thank Monash University for supporting the analogue modelling laboratory. Thierry Menand, Agust Gudmundsson and the editor Rob Govers are thanked for their thoughtful reviews which have helped to improve the manuscript. Andrew Bunger and Dan Faulkner are thanked for helpful discussions, Pete Kokelaar is thanked for comments on a previous version of the manuscript.

Tables

	<i>Geometry</i>	<i>Material</i>	<i>m</i>	<i>a</i>
Load A	Cylinder	Brass	0.0501	0.0125
Load B	Cylinder	Brass	0.0418	0.0125

Table 1. Properties of experimental loads used to calculate Young's modulus E , where ' m ' is the mass of the load (kg) and ' a ' is its radius (m). The averaged measurements of E are reported in Table 3.

	X_1	X_2	M_1	M_2	D_1	D_2	T_s	T_m	<i>Int type</i>	T	t	Q	<i>Intrusion formed</i>
<i>Large Tank Experiments</i>													
LBR2	2.5	2.5	20	20	11.2	12.6	5	21.3	O	7.5	116	3.9	Dyke-sill hybrid
LBR4	2.5	2.5	20	20	11.4	12.4	5	20.3	C	6.8	124	3.9	Sill
LBR5	2.5	2.5	20	20	11.4	12.9	5	19.4	C	6.9	167	3.9	Sill
LBR6	2.5	2.5	20	20	11.5	12.2	5	20.0	C	6.8	168	3.9	Dyke-sill hybrid
MOPIV6	2.5	3	20	20	12.2	12.4	5	22.0	C	7.6	67	3.9	Dyke-sill hybrid
MOPIV9	2.5	2.5	20	20	12.5	12.5	5	21.0	C	6.7	66	3.9	Sill
<i>Small Tank Experiments</i>													
SBR17	2.5	2.5	3	2	10.6	7.2	5	22.3	C	6.9	121	3.9	Dyke-sill hybrid
SBR18	2.5	2.5	3	2	10.3	7.7	5	24.2	C	6.1	121	3.9	Dyke erupted
SBR19	2.5	2.5	3	2	10.7	7.3	5	22.0	C	6.0	121	3.9	Sill
SBR20	2.5	2.5	3	2	10.6	7.8	5	23.0	C	6.4	122	3.9	Sill
SBR21	2.5	2.5	3	2	10.7	7.7	5	21.7	C	6.6	122	3.9	Dyke-sill hybrid

Table 2. Parameters, variables and intrusions forms of the ‘large’ and ‘small’ tank experiments. X (wt%) = gelatine concentration, M (kg) = mass of gelatine-water mixture used in each layer, D (cm) = thickness of gelatine layer, T_s (°C) = temperature of solid gelatine layer 1 immediately prior to pouring layer 2 in place during experiment preparation, T_m (°C) = mixture temperature of layer 2 gelatine when poured on to cooled layer 1, ‘*Int type*’ refers to the method used to prepare the interface between gelatine layers where C = cling-wrap and O = oiled, T (°C) = temperature of gelatine solids at time of running the experiment, t (hours) = amount of time gelatine has been curing in the refrigerator (layer 2, where layer 1 has cured for ~24 hours longer), and Q ($\times 10^{-7}$ m³/s) volumetric flow rate (flux) of injected fluid. Subscripts 1 and 2 refer to the lower and upper gelatine layers, respectively.

	E_2	E_2/E_1	K_{IcG}	K_{IcInt}	K_{Ic}^*
LBR2	6201	1	116	69	0.66
LBR4	5758	1	89	53	0.51
LBR5	5546	1	103	33	0.32
LBR6	5885	1	109	56	0.54
MOPIV6	7740	1.42	67	23	0.22
MOPIV9	5170	1	100	45	0.43
SBR17	6527	1	90	68	0.65
SBR18	5922	1	83	-	1^
SBR19	7076	1	107	62	0.59
SBR20	8204	1	122	50	0.48
SBR21	8777	1	-	-	-

Table 3. Results from experiments where fluid was injected at a constant volumetric flow rate (flux). E (Pa) = Young's modulus (+/- 10%; average measurement recorded, using two different experimental loads (Table 1)), E_2/E_1 = model ratio of Layer 2 and Layer 1 Young's moduli assuming gelatine has cured (see Kavanagh et al., 2013), K_{Ic} (Pa m^{0.5}) = fracture toughness calculated assuming pressure equilibrium. Subscripts l and 2 refer to the lower and upper gelatine layers, respectively, ' G ' refers to a gelatine layer 1 and ' int ' refers to the interface. $K_{Ic}^* = K_{IcInt} / \text{average } K_{IcG}$ (average $K_{IcG} = 103$ Pa m^{0.5} (large tank) or 106 Pa m^{0.5} (small tank) for sill or dyke-sill hybrid-forming experiments where $E_2 = E_1$). As SBR21 failed the pressure-equilibrium criteria, its K_{IcG} and K_{IcInt} could not be calculated. ^Estimated value as K_{IcInt} could not be measured in this dyke-forming experiment.

Figures

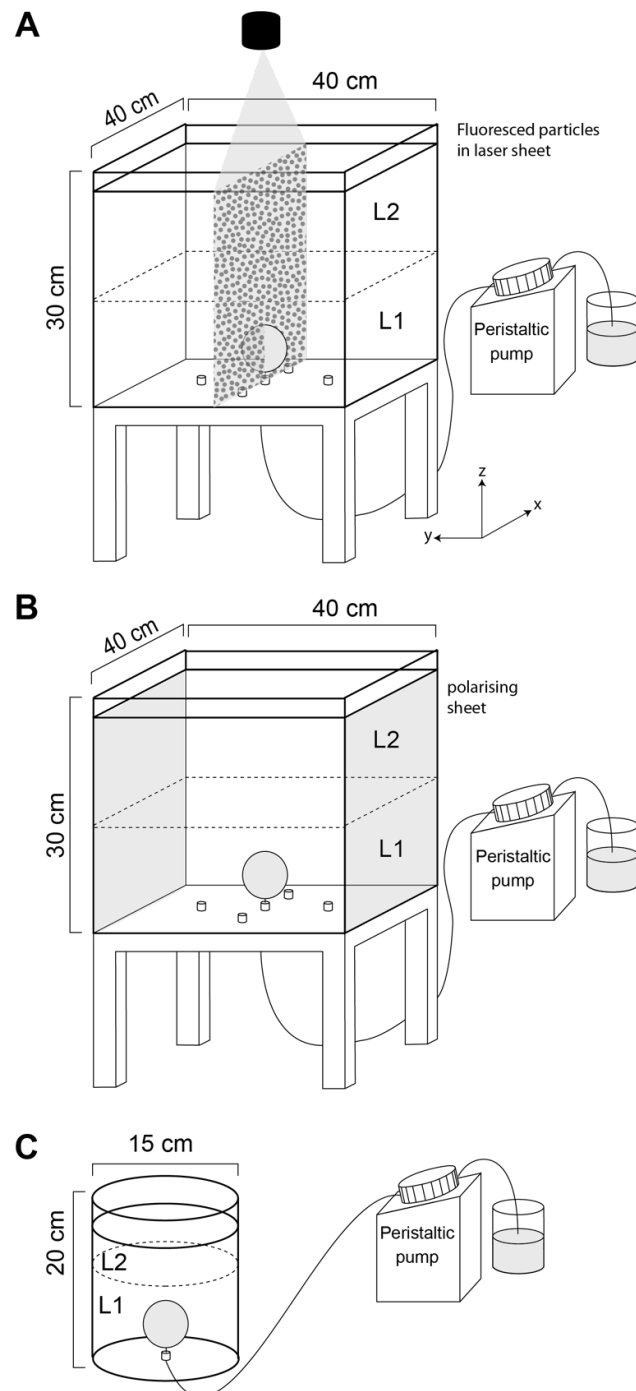


Figure 1. Schematic illustration of experiment apparatus and setup of two-layered gelatine experiments injected with water by a peristaltic pump. A) Neutrally-buoyant particles were added to the gelatine during its preparation; these fluoresced when intersected by an overhead thin, vertical laser sheet oriented parallel to the feeder dyke's thickness during the experiment. B) Polarised sheets were fitted to the exterior of the tank, the gelatine's photoelasticity produced colour fringes of stress concentration during fluid injection. The clear-Perspex experiment containers were 'large' 30 cm high and 40 cm square (A, B), or 'small' 15 cm diameter cylinders (C).

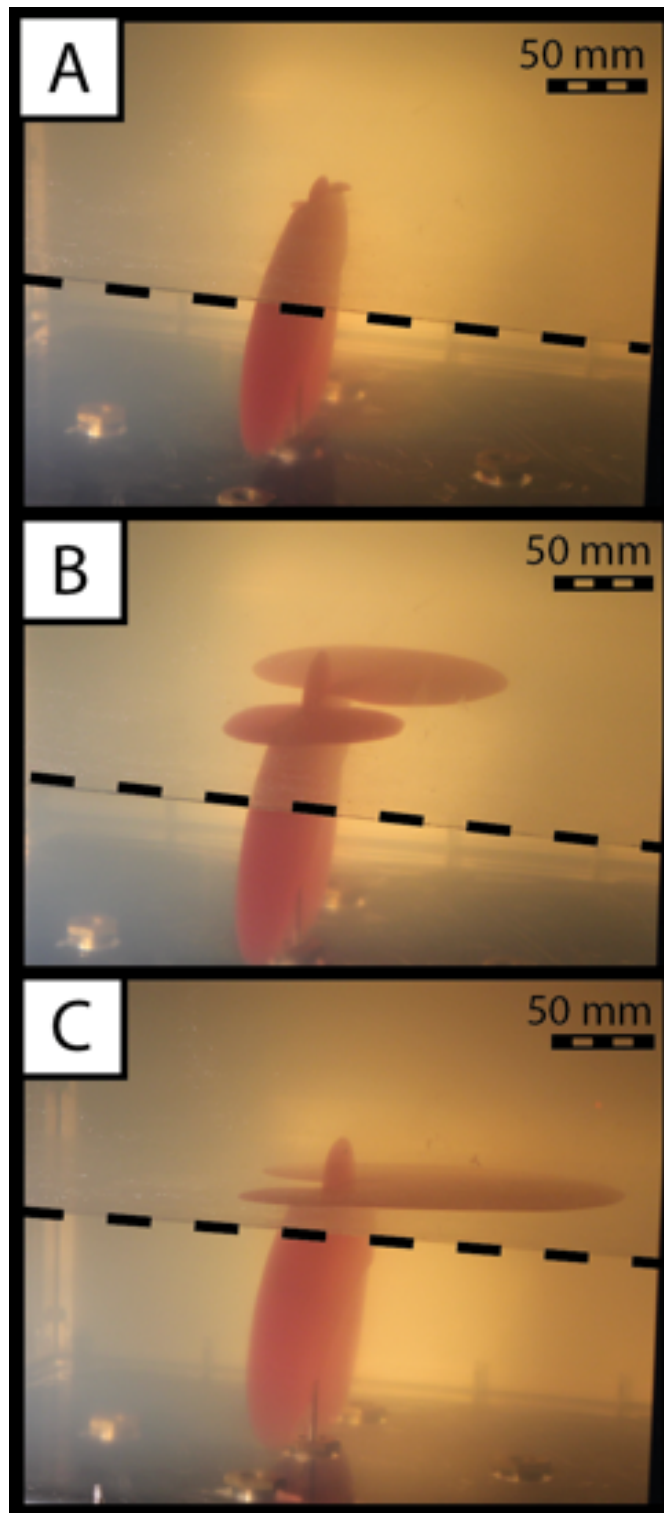


Figure 2. Dyke-sill hybrid formation (LBR2) in one of the ‘large’ tank experiments. The intrusion is viewed looking down and from the side, onto the interface between the gelatine layers. The position of the interface against the tank wall is indicated by the dashed line. A) A penny-shaped dyke has propagated through the lower gelatine layer and slightly protruded into the upper layer, with two small sills intruding the horizontal interface where it is intercepted by the dyke margins. B) The dyke protrusion in the upper layer quickly became arrested as the sills grew. C) The sills joined together within the interface, continued to grow and then coalesced with one margin of the dyke to create the final dyke-sill hybrid structure.

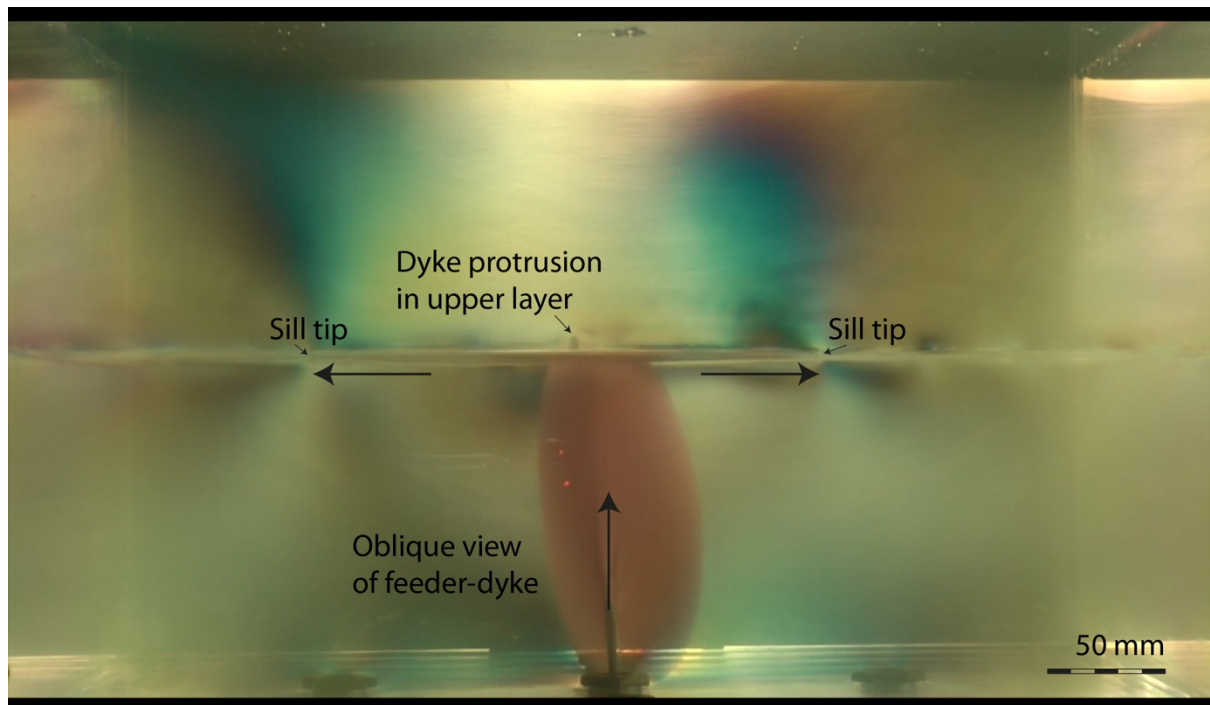


Figure 3. Video of dyke-sill hybrid formation (experiment LBR6). The intrusion is viewed with polarised light, approximately perpendicular to the strike direction of the dyke. Interference colours indicate the evolving distribution and intensity of stress within the gelatine host.

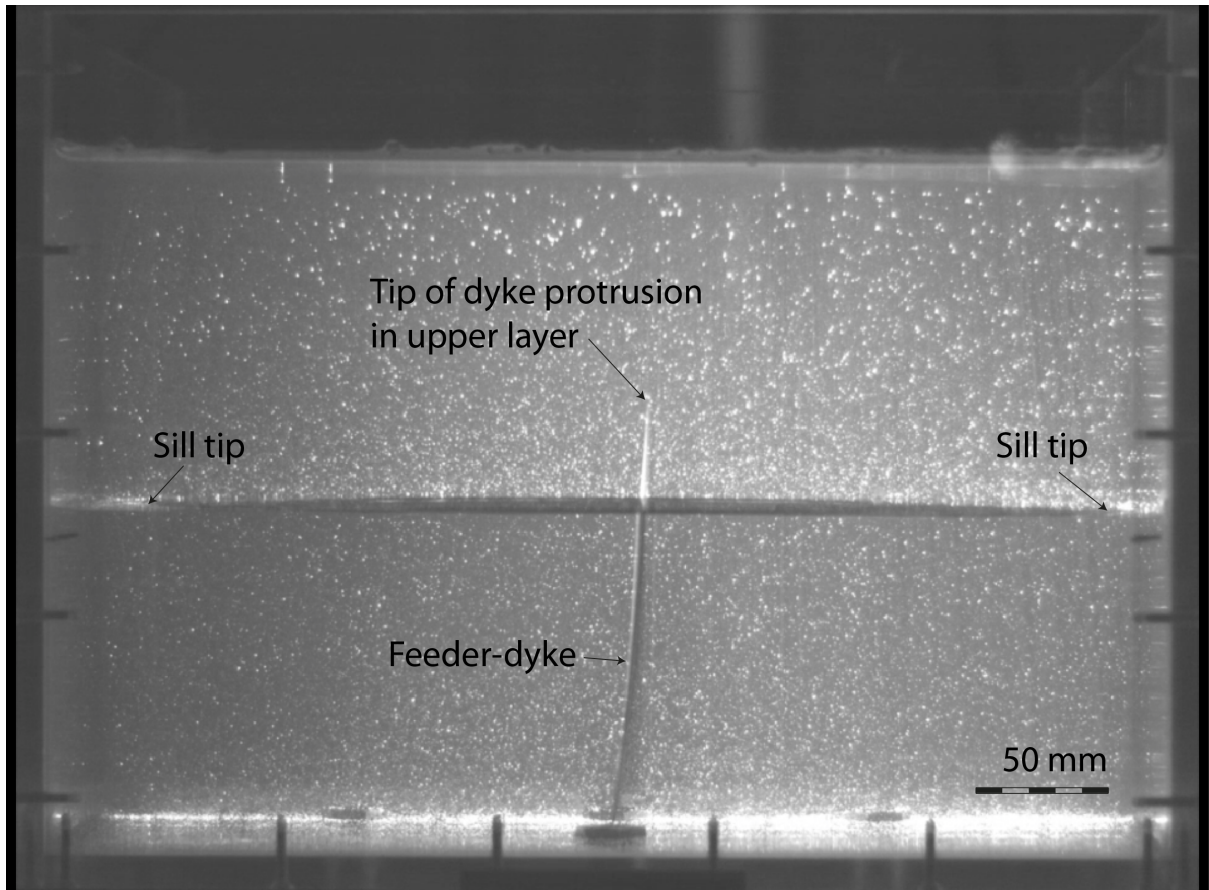


Figure 4. Dyke-sill hybrid formation, with fluorescent particles in the gelatine illuminated by a thin vertical laser sheet (experiment MOPIV6). Video compiled from successive images collected with a CCD camera. The intrusion is viewed perpendicular to the dyke strike direction.

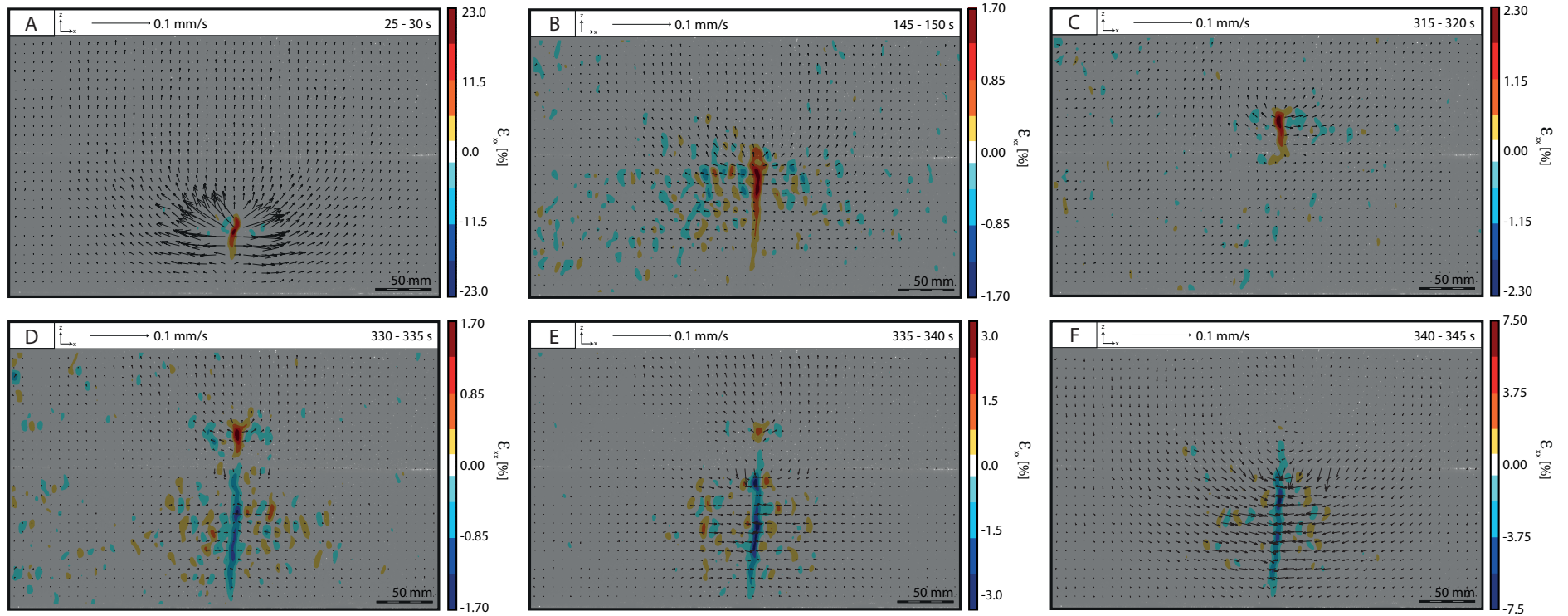


Figure 5. Video showing digital image correlation (DIC) model of dyke-sill hybrid formation (MOPIV6), plotting incremental strain ϵ_{xx} (at 5-second intervals). Selected time frames of incremental strain evolution in the gelatine host during dyke-sill hybrid formation are shown in A-F. The black vector arrows indicate the direction and magnitude of gelatine displacement, and the colour-map indicates the calculated incremental strain (ϵ_{xx} %). The experimental intrusion is viewed perpendicular to the dyke strike direction. A) 25-30 s, B) 145-150 s, C) 315-320 s, D) 330-335 s, E) 335-340 s, and F) 340-345 s.

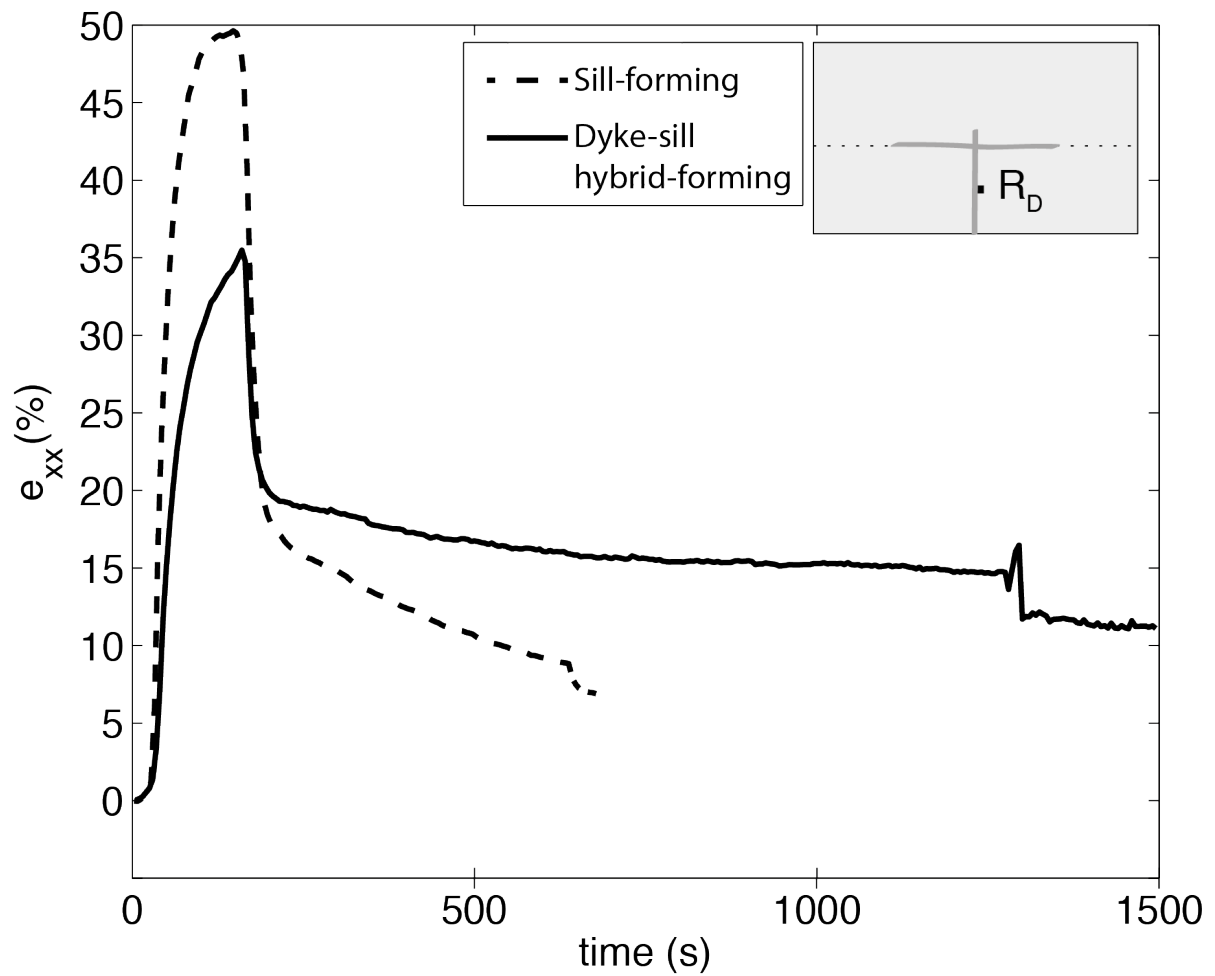


Figure 6. Evolution of finite strain (e_{xx} %) in a 5 mm x 5 mm area adjacent to the feeder dyke of a dyke-sill hybrid experiment (MOPIV6) and a sill-forming experiment (MOPIV9). In both experiments at the moment of sill formation and feeder dyke contraction (160-165 seconds) there was a rapid decrease in e_{xx} , though this decrease was greater in the sill-forming experiment than the dyke-sill hybrid one.

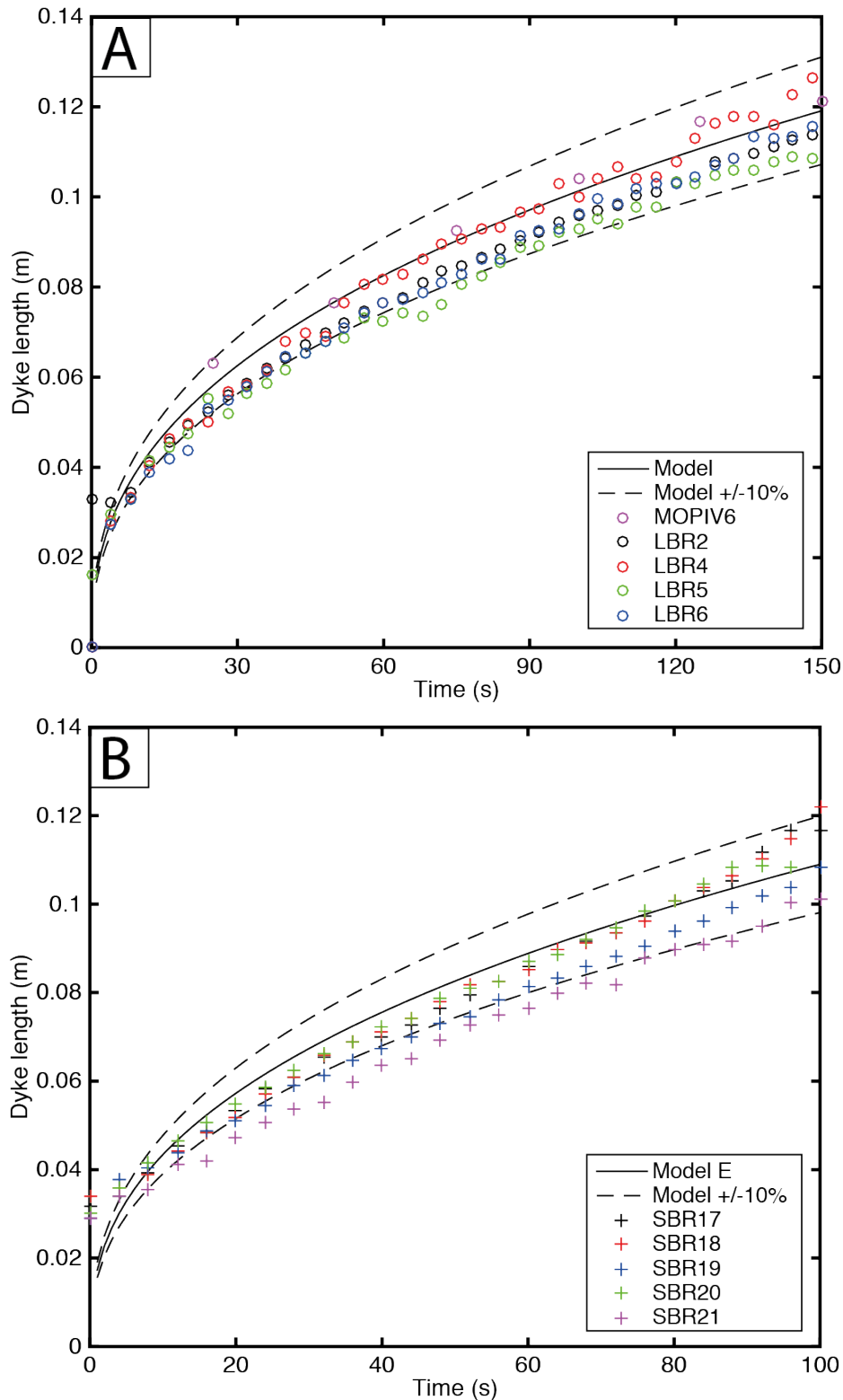


Figure 7. Dyke length (± 0.002 m, approximately the length of the symbol) versus time in large and small tank experiments. The model (solid-line) defines the geometry expected if the injections are in fracture toughness pressure equilibrium ($\pm 10\%$ uncertainty, dashed-lines). A) Large tank experiments, Young's modulus $E = 5850$ Pa and fracture toughness $K_{IcG} = 104$ Pa $m^{0.5}$, B) small tank experiments $E = 7300$ Pa and $K_{IcG} = 108$ Pa $m^{0.5}$. In both cases the models assume constant flux $Q = 3.9 \times 10^{-7}$ m³/s. Most of the experimental measurements lie within the dashed lines and so indicate the assumption of equilibrium is valid, excluding SBR21.

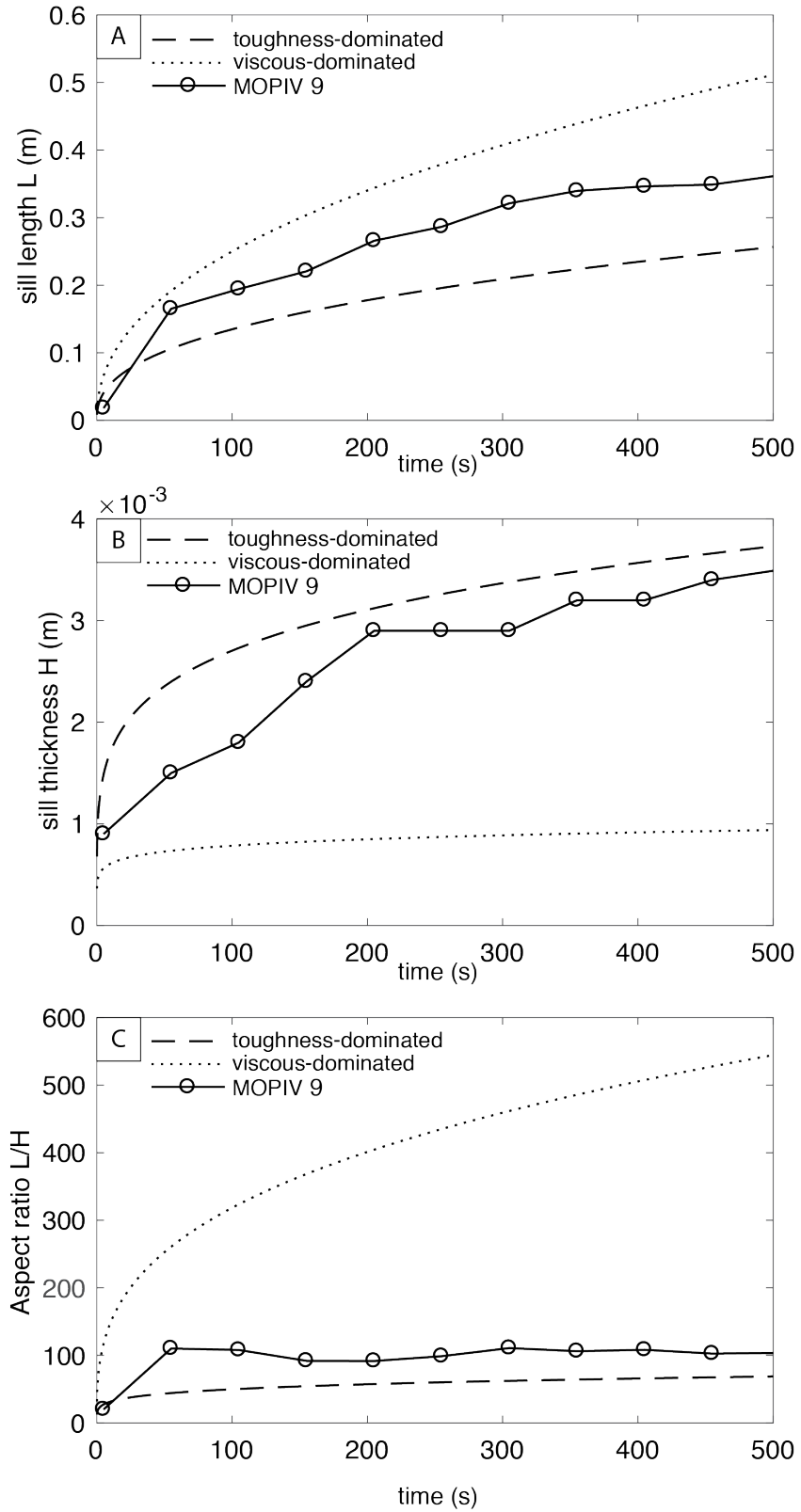


Figure 8. Sill length (A), thickness (B) and aspect ratio (C) (solid line, ± 0.002 m) versus time from experiment MOPIV9. Two equilibrium models are shown which define the sill geometry expected if the injections are in a toughness-dominated regime (dashed line) or viscosity-dominated regime (dotted line). $E = 5170$ Pa, $K_{IcInt} = 45$ Pa $m^{0.5}$, $Q = 3.9 \times 10^{-7}$ m³/s and $\mu = 8.9 \times 10^{-7}$ Pa s.

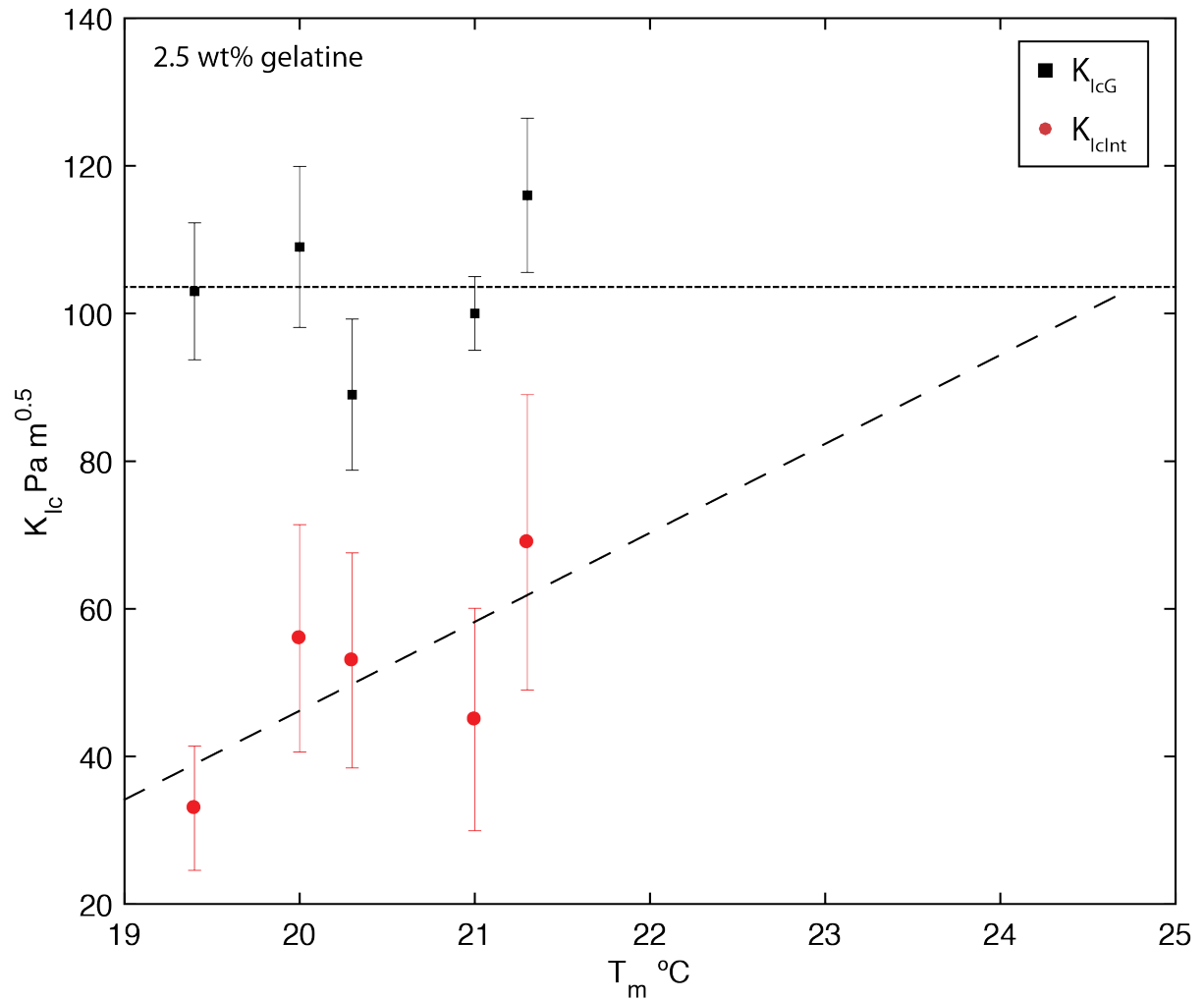


Figure 9. Fracture toughness of the upper gelatine layer K_{IcG} and interface fracture toughness K_{IcInt} plotted against T_m (the preparation temperature of the upper layer when poured in place). Average K_{IcG} is indicated as 103 Pa m^{0.5}. T_m and K_{Ic} of the interface are positively correlated, and the dashed-line shows the line of best fit $K_{IcInt} = 12.1 * T_m - 197$ ($R^2 = 0.48$). Only the results from large tank experiments are shown; $X_1 = X_2 = 2.5$ wt%, and $E_2 = E_1$.

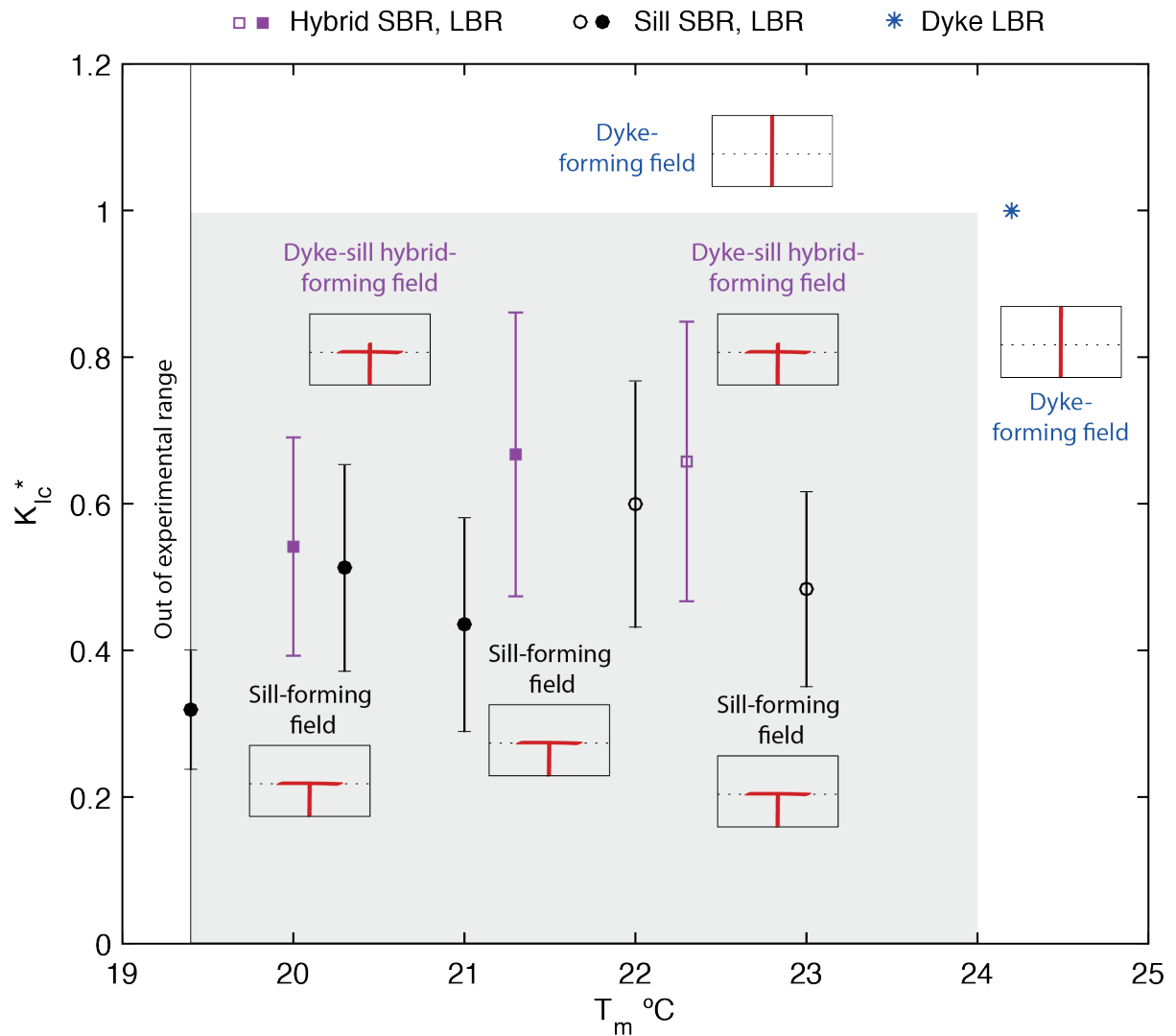


Figure 10. Experimental intrusion form T_m and K_{Ic}^* (hybrid - purple squares: open SBR, filled LBR; sill - black circles: open SBR, filled LBR, or dyke - blue star: LBR; see Tables 2 and 3 for details). The unshaded region indicates the field of dyke formation where $T_m \geq 19.4$ °C and $K_{Ic}^* \geq 1$, and $T_m > 24$ °C. The shaded region indicates sill-forming and hybrid-forming fields, both occur where $T_m < 24$ °C and $K_{Ic}^* < 1$. Sill formation is associated with relatively low K_{Ic}^* (low K_{IcInt} relative to K_{IcG}). Only experiments with 2.5 wt% concentration gelatine layers are shown, where $E_2 = E_1$. $T_m < 19.4$ °C was not possible experimentally.

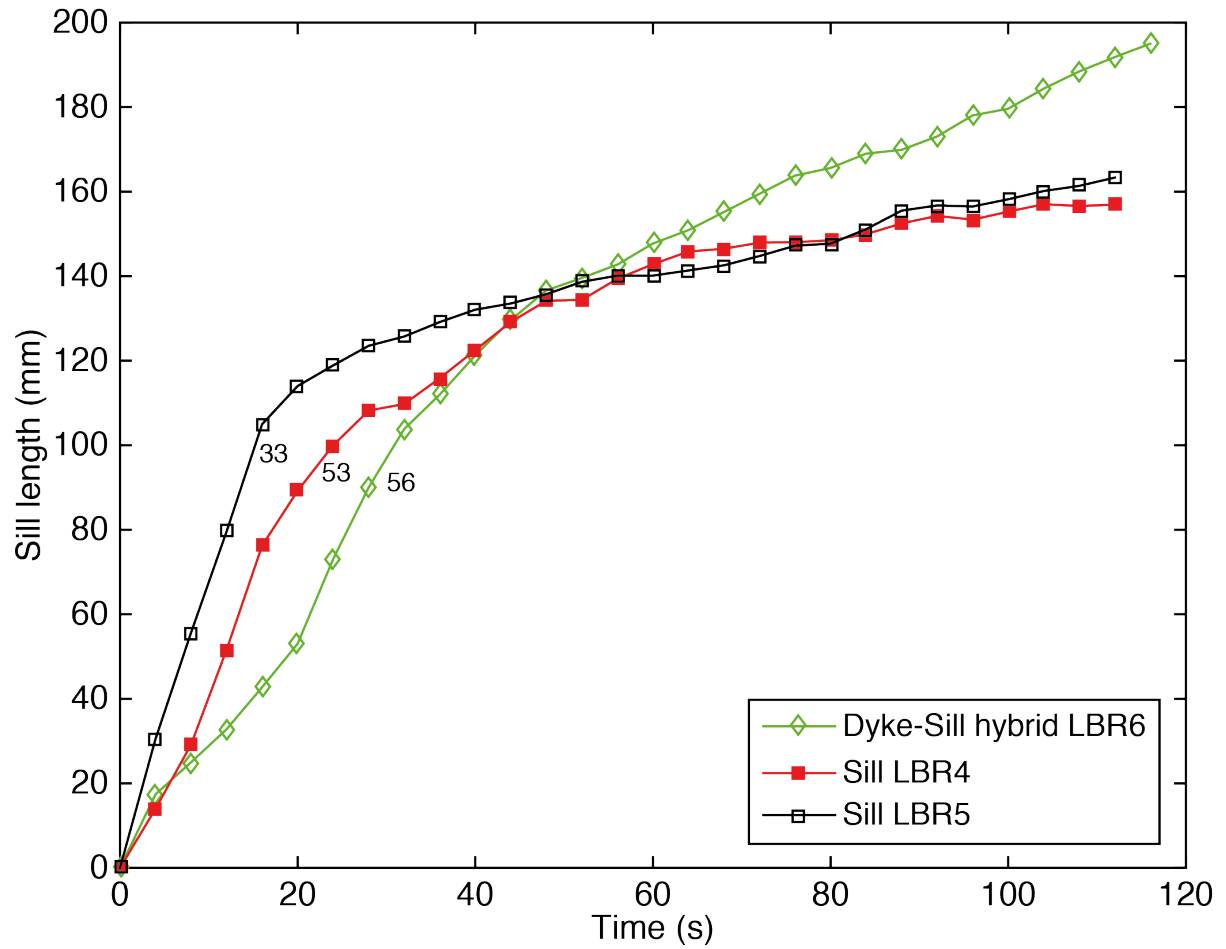


Figure 11. Sill length (+/- 2mm, ~ symbol size) versus time (s) since sill inception in three large-tank experiments that are sill-forming (squares, LBR4 and LBR5) and dyke-sill hybrid-forming (diamonds, LBR6). The calculated fracture toughness of the interface K_{IcInt} intruded by the sill is indicated, showing that sills grew faster when the interface fracture toughness was lower.

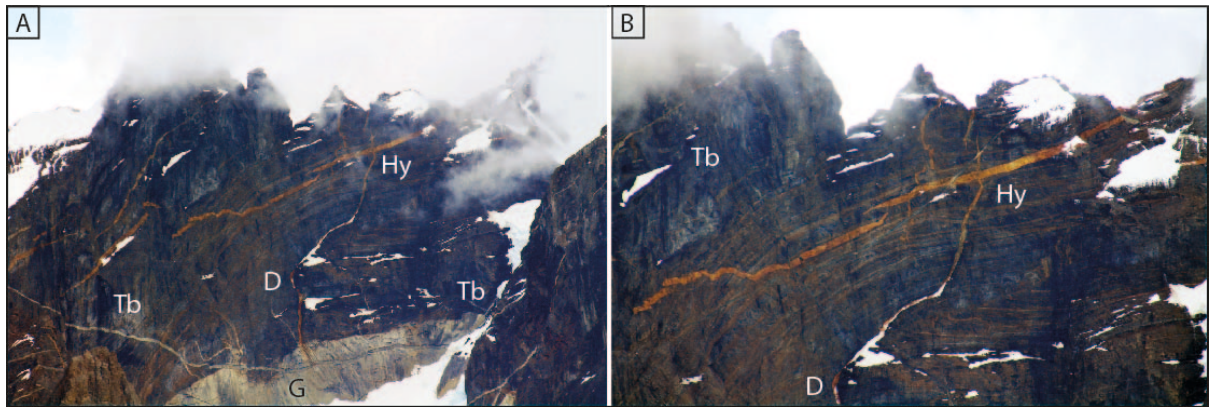


Figure 12. Photographs of felsic intrusions within a folded turbidite sequence in Las Torres del Paine National Park, Chile. A) Roof contact of a large grey/white granite laccolith (G), where the overlying turbidite sequence (Tb) has been intruded by felsic dykes (D), sills and hybrid (Hy) intrusions that have weathered orange and are approximately 15 m thick. The image shows approximately 600 m of vertical extent. B) Zoomed section of A). The small intrusions are thought to be associated with the growth of the laccolith.

References

- Adam, J. et al., 2005. Shear localisation and strain distribution during tectonic faulting---new insights from granular-flow experiments and high-resolution optical image correlation techniques. *Journal of Structural Geology*, 27(2), pp.283–301.
- Anderson, E.M., 1938. The dynamics of sheet intrusion. *Proceedings of the Royal Society of Edinburgh*, 58(3), pp.242–251.
- Annen, C. et al., 2015. Construction and evolution of igneous bodies: Towards an integrated perspective of crustal magmatism. *Lithos*, 230(C), pp.206–221.
- Annen, C., Blundy, J.D. & Sparks, R.S.J., 2006. The Genesis of Intermediate and Silicic Magmas in Deep Crustal Hot Zones. *Journal of Petrology*, 47(3), pp.505–539.
- Barnes S.J., Cruden A., Arnt N., and Saumur B. 2016. The mineral system approach applied to magmatic Ni-Cu-PGE sulfide deposits. *Ore Geology Reviews*, 76, 296-316.
- Blundy, J. et al., 2015. Generation of porphyry copper deposits by gas–brine reaction in volcanic arcs. *Nature Geoscience*, 8(3), pp.235–240.
- Brown, R.J. et al., 2007. Mechanically disrupted and chemically weakened zones in segmented dike systems cause vent localization: Evidence from kimberlite volcanic systems. *Geology*, 35(9), pp.815–818.
- Bunger, A.P. & Cruden, A.R., 2011. Modeling the growth of laccoliths and large mafic sills: Role of magma body forces. *Journal of Geophysical Research*, 116(B02203), doi:10.1029–2010JB007648.
- Chanceaux, L. & Menand, T., 2014. Solidification effects on sill formation: An experimental approach. *Earth and Planetary Science Letters*, 403(C), pp.79–88.
- Chanceaux, L. & Menand, T., 2016. The effects of solidification on sill propagation dynamics and morphology. *Earth and Planetary Science Letters*, 442, pp.39–50.
- Coleman, D.S., Gray, W. & Glazner, A.F., 2004. Rethinking the emplacement and evolution of zoned plutons: Geochronologic evidence for incremental assembly of the Tuolumne Intrusive Suite, California. *Geology*, 32(5), pp.433–436.
- Corry, C.E., 1988. Laccoliths: mechanics of emplacement and growth. *Geological Society of America Special Paper*, 220.
- Crisp, J.A., 1984. Rates of magma emplacement and volcanic output. *Journal of Volcanology and Geothermal Research*, 20, pp.177–211.
- Cruden, A.R. & McCaffrey, K.J.W., 2001. Growth of plutons by floor subsidence: implications for rates of emplacement, intrusion spacing and melt-extraction mechanisms. *Physics and Chemistry of the Earth, Part A*, 26(4-5), pp.303–315.
- Daniels, K.A. & Menand, T., 2015. An experimental investigation of dyke injection under regional extensional stress. *Journal of Geophysical Research*, 120(3), pp.2014–2035.

- Daniels, K.A. et al., 2012. The shapes of dikes: evidence for the influence of cooling and inelastic deformation. *GSA Bulletin*, 124(7-8), pp.1102–1112.
- Delaney, P.T. et al., 1986. Field relations between dikes and joints: Emplacement processes and palaeostress analysis. *Journal of Geophysical Research*, 91(B5), pp.4920–4938.
- Di Giuseppe, E. et al., 2009. Gelatins as rock analogs: A systematic study of their rheological and physical properties. *Tectonophysics*, 473(3-4), pp.391–403.
- Fiske, R.S. & Jackson, E.D., 1972. Orientation and Growth of Hawaiian Volcanic Rifts: The Effect of Regional Structure and Gravitational Stresses. *Proceedings of the Royal Society A: Mathematical, Physical and Engineering Sciences*, 329(1578), pp.299–326.
- Galland, O., Holohan, E.P., Van Wyk De Vries, B. & Burchardt, S., 2015. Laboratory modelling of Volcano Plumbing Systems: A Review. In *Advance in Volcanology*. Springer, pp. 1–68.
- Gernon, T.M., Field, M. & Sparks, R.S.J., 2012. Geology of the Snap Lake kimberlite intrusion, Northwest Territories, Canada: field observations and their interpretation. *Journal of the Geological Society*, 169(1), pp.1–16.
- Geshi, N., Kusumoto, S. & Gudmundsson, A., 2012. Effects of mechanical layering of host rocks on dike growth and arrest. *Journal of Volcanology and Geothermal Research*, 223-224(C), pp.74–82.
- Glazner, A.F. et al., 2004. Are plutons assembled over millions of years by amalgamation from small magma chambers? *GSA Today*, 14(4), pp.4–11.
- Gudmundsson, A., 1983. Form and dimensions of dykes in eastern Iceland. *Tectonophysics*, 95(3-4), pp.295–307.
- Gudmundsson, A., 2002. Emplacement and arrest of sheets and dykes in central volcanoes. *Journal of Volcanology and Geothermal Research*, 116, pp.279–298.
- Gudmundsson, A. & Brenner, S.L., 2005. On the conditions of sheet injections and eruptions in stratovolcanoes. *Bulletin of volcanology*, 67(8), pp.768–782.
- Gudmundsson, A., 2011. Deflection of dykes into sills at discontinuities and magma-chamber formation. *Tectonophysics*, 500(1-4), pp.50–64.
- Gudmundsson, A. & Løtveit, I.F., 2014. Sills as fractured hydrocarbon reservoirs: examples and models. In *Geological Society, London, Special Publications*, 374(1), 251-271.
- Holness, M.B. & Humphreys, M.C.S., 2003. The Traigh Bhan na Sgurra Sill, Isle of Mull: Flow Localization in a Major Magma Conduit. *Journal of Petrology*, 44(11), pp.1961–1976.
- Hubbert, M.K., 1937. Theory of scale models as applied to the study of geologic structures. *Bulletin of the Geological Society of America*, 48(10), pp.1459–1517.
- Hyndman, D.W. & Alt, D., 1987. Radial dikes, laccoliths, and gelatin models. *Journal of Geology*, 95, pp.763–774.

- Kavanagh, J., Menand, T. & Daniels, K.A., 2013. Gelatine as a crustal analogue: Determining elastic properties for modelling magmatic intrusions. *Tectonophysics*, 582, pp.101–111.
- Kavanagh, J.L. & Pavier, M.J., 2014. Rock interface strength influences fluid-filled fracture propagation pathways in the crust. *Journal of Structural Geology*, 63, pp.68–75.
- Kavanagh, J.L. & Sparks, R.S.J., 2011. Insights of dyke emplacement mechanics from detailed 3D dyke thickness datasets. *Journal of the Geological Society*, 168(4), pp.965–978.
- Kavanagh, J.L., Boutelier, D. & Cruden, A.R., 2015. The mechanics of sill inception, propagation and growth: Experimental evidence for rapid reduction in magmatic overpressure. *Earth and Planetary Science Letters*, 421, pp.117–128.
- Kavanagh, J.L., Menand, T. & Sparks, R.S.J., 2006. An experimental investigation of sill formation and propagation in layered elastic media. *Earth and Planetary Science Letters*, 245(3-4), pp.799–813.
- Le Corvec, N. et al., 2013. Spatial distribution and alignments of volcanic centers: Clues to the formation of monogenetic volcanic fields. *Earth-Science Reviews*, 124(C), pp.1–19.
- Le Corvec, N., McGovern, P.J. & Grosfils, E.B., 2015. Effects of crustal-scale mechanical layering on magma chamber failure and magma propagation within the Venusian lithosphere. *Journal of Geophysical Research: Planets*, 120(7), pp.1279–1297.
- Leuthold, J. et al., 2012. Time resolved construction of a bimodal laccolith (Torres del Paine, Patagonia). *Earth and Planetary Science Letters*, 325-326, pp.85–92.
- Lister, J.R. & Kerr, R.C., 1991. Fluid-Mechanical Models of Crack Propagation and Their Application to Magma Transport in Dyke. *Journal of Geophysical Research*, 96, pp.10049–10077.
- Loughlin, S.C. et al. eds., 2015. *Global Volcanic Hazards and Risk*, Cambridge, UK: Cambridge University Press.
- Magee, C., Jackson, C.A.L. & Schofield, N., 2013. The influence of normal fault geometry on igneous sill emplacement and morphology. *Geology*, 41(4), pp.407–410.
- Malthe-Sørensen, A. et al., 2004. Formation of saucer-shaped sills. *Physical geology of high-level magmatic systems*. Geological Society, London, Special Publications, 234, pp.215–227.
- Menand, T. & Tait, S.R., 2002. The propagation of a buoyant liquid-filled fissure from a source under constant pressure: An experimental approach. *Journal of Geophysical Research*, 107(2306), pp.177–185.
- Merle, O., 2015. The scaling of experiments on volcanic systems. *Frontiers in Earth Science*, 3, 26.
- Michaut, C., 2011. Dynamics of magmatic intrusions in the upper crust: Theory and applications to laccoliths on Earth and the Moon. *Journal of Geophysical Research*, 116(B05205).

- Muirhead, J.D. et al., 2014. Cracking the lid: Sill-fed dikes are the likely feeders of flood basalt eruptions. *Earth and Planetary Science Letters*, 406(C), pp.187–197.
- Naldrett, A.J., 2011. Fundamentals of magmatic sulfide deposits. *Reviews in Economic Geology*, 17, pp.1–50.
- Poland, M.P., Fink, J.H. & Tauxe, L., 2004. Patterns of magma flow in segmented silicic dikes at Summer Coon volcano, Colorado: AMS and thin section analysis. *Earth and Planetary Science Letters*, 219(1-2), pp.155–169.
- Pollard, D.D. & Johnson, A.M., 1973. Mechanics of growth of some laccolithic intrusions in the Henry mountains, Utah, II: Bending and failure of overburden layers and sill formation. *Tectonophysics*, 18(3-4), pp.311–354.
- Polteau, S. et al., 2008. How are saucer-shaped sills emplaced? Constraints from the Golden Valley Sill, South Africa. *Journal of Geophysical Research*, 113(B12), B12104.
- Richardson, J.A. et al., 2015. Role of sills in the development of volcanic fields: Insights from lidar mapping surveys of the San Rafael Swell, Utah. *Geology*, 43(11), pp.1023–1026.
- Rivalta, E. et al., 2015. A review of mechanical models of dike propagation: Schools of thought, results and future directions. *Tectonophysics*, 638, pp.1–42.
- Rivalta, E., Böttlinger, M. & Dahm, T., 2005. Buoyancy-driven fracture ascent: Experiments in layered gelatine. *Journal of Volcanology and Geothermal Research*, 144(1-4), pp.273–285.
- Roberts, J.L., 1970. The intrusion of magma into brittle rocks J. L. Roberts, ed. Mechanism of igneous intrusion. Gallery Press, Liverpool, pp.287–338.
- Rocchi, S. et al., 2010. Intrusive sheets and sheeted intrusions at Elba Island, Italy. *Geosphere*, 6(3), pp.225–236.
- Savitski, A.A. & Detournay, E., 2002. Propagation of a penny-shaped fluid-driven fracture in an impermeable rock: asymptotic solutions. *International Journal of Solids and Structures*, 39, pp.6311–6337.
- Schrank, C.E., Boutelier, D.A. & Cruden, A.R., 2008. The analogue shear zone: From rheology to associated geometry. *Journal of Structural Geology*, 30(2), pp.177–193.
- Sigmundsson, F. et al., 2010. Intrusion triggering of the 2010 Eyjafjallajökull explosive eruption. *Nature*, 468(7322), pp.426–430.
- Sigmundsson, F. et al., 2014. Segmented lateral dyke growth in a rifting event at Ba'rdarbunga volcanic system, Iceland. *Nature*, 517(7533), pp.191–195.
- Svensen, H. et al., 2004. Release of methane from a volcanic basin as a mechanism for initial Eocene global warming. *Nature*, 429(6991), pp.542–245.
- Taisne, B. & Jaupart, C., 2009. Dike propagation through layered rocks. *Journal of Geophysical Research-Solid Earth*, 114(B9), doi:10.1029–2008JB006228.

- Taisne, B. & Tait, S., 2009. Eruption versus intrusion? Arrest of propagation of constant volume, buoyant, liquid-filled cracks in an elastic, brittle host. *Journal of Geophysical Research*, 114(B6), B06202.
- Taisne, B. & Tait, S., 2011. Effect of solidification on a propagating dike. *Journal of Geophysical Research*, 116(B1), B01206.
- Takada, A., 1990. Experimental study on propagation of liquid-filled crack in gelatin: shape and velocity in hydrostatic stress condition. *Journal of Geophysical Research*, 95, pp.8471–8481.
- Tarasewicz, J. et al., 2012. Using microearthquakes to track repeated magma intrusions beneath the Eyjafjallajökull stratovolcano, Iceland. *Journal of Geophysical Research*, 117(B00C06), doi:10.1029–2011JB008751.
- Thomson, K. & Schofield, N., 2008. Lithological and structural controls on the emplacement and morphology of sills in sedimentary basins. *Geological Society London Special Publications*, 302(1), pp.31–44.
- van Otterloo, J. & Cruden, A.R., 2016. Rheology of pig skin gelatine: Defining the elastic domain and its thermal and mechanical properties for geological analogue experiment applications. *Tectonophysics*, 683, pp.86–97.
- White, J.L. et al., 2012. Kimberlite sills and dykes associated with the Wesselton Kimberlite Pipe, Kimberley, South Africa. *South African Journal of Geology*, 115(1), pp.1–32.
- White, R.S. et al., 2011. Dynamics of dyke intrusion in the mid-crust of Iceland. *Earth and Planetary Science Letters*, 304(3-4), pp.300–312.